Characterization of Third Order Nonlinearities in TiO_2 Waveguides at 1550 nm

by

Katia Shtyrkova

B.S. Optical Sciences and Engineering, 2009
University of Arizona
Tucson, AZ, USA

Submitted to the Department of Electrical Engineering and Computer Science
in Partial Fulfillment of the Requirements for the Degree of

Master of Science in Electrical Engineering and Computer Science

at the

MASSACHUSETTS INSTITUTE OF TECHNOLOGY

February 2013

Author .....
Department of Electrical Engineering and Computer Science
January 31, 2013

Certified by .....
Erich P. Ippen
Elihu Thomson Professor of Electrical Engineering
Professor of Physics
Thesis Supervisor

Accepted by .....
Leslie A. Kolodziejski
Chair, Department Committee on Graduate Students

Characterization of Third Order Nonlinearities in TiO_2 Waveguides at 1550 nm

by

Katia Shtyrkova

Submitted to the Department of Electrical Engineering and Computer Science
on January 31, 2013, in partial fulfillment of the
requirements for the Degree of
Master of Science in Electrical Engineering and Computer Science

Abstract

Polycrystalline anatase titanium dioxide waveguides are investigated as an alternative material for all-optical switching at telecommunications C-band wavelengths. Titanium dioxide does not support two-photon absorption at 1550 nm, has a high refractive index, and a relatively low loss, which allows for high-index-contrast waveguides. The TiO_2 waveguides studied for this thesis were single-mode, with dimensions $200nm \times 900nm$, deposited on oxidized silicon and overclad with a transparent polymer. The optical Kerr coefficient was measured using two methods: spectral broadening studies and heterodyne pump-probe experiments. The spectral broadening studies indicated an optical Kerr coefficient of $n_2 = 1.82 \times 10^{15} cm^2/W$, while the heterodyne pump-probe experiments, yielded a value of $n_2 = 1.03 \times 10^{15} cm^2/W$. Both techniques and their implementation are described in detail. Split-step code simulations including dispersion and linear loss as well as nonlinearity confirm the internal consistency of each experiment separately. Further experiments are needed to resolve the remaining difference.

Thesis Supervisor: Erich P. Ippen
Title: Elihu Thomson Professor of Electrical Engineering
Professor of Physics

Acknowledgments

This thesis would not have been possible without several remarkable people, whom I have been fortunate enough to meet/work with.

First and foremost, I would like to thank my graduate advisor, Professor Erich P. Ippen. I have been told multiple times that having the right advisor is more important than having the right research project. Professor Ippen is the best advisor one could have, and every one of his students would confirm this. Thank you, Professor Ippen, for all your support, for all the time you always have for scientific discussion; thank you giving me the freedom to do what I love to do, thank you for your encouragement, thank you for your neverending scientific knowledge and for sharing some of it with me. I love every day that I spend at MIT, I love my research projects, and I sincerely love my lab (hence my co-workers from your group have named me "a true believer"), and that is mostly because of the work environment that you have created for your students. I am extremely fortunate and proud to be your student. I will be honored, and I look forward to having your signature on my PhD thesis (however far away this might be). Thank you.

Thank you to Christopher Evans, Jonathan Bradley, Orad Reshef, and Professor Eric Mazur from Harvard, for collaborating with me on TiO_2 waveguides work. Thank you for giving me the opportunity to work on this project. Chris, you have been the best collegue I have ever had. Your work ethics, your immediate and open williness to help, and your scientific and experimental knowledge are formidable. I have learned a lot from you, I hope I will learn more in the future. Thank you.

Thank you to Ali Motamedi, for teaching me most everything that I know about pump-probe experiments. Thank you for all the late evenings and weekends that you spent in the lab with me, after you had already graduated from MIT; thank you for all your explanations, for endless meetings, and for numerous phone calls and e-mails. Thank you for passing your knowledge along to me.

Thank you to Marcus Dahlem for teaching me the basics of the microphotonics measurements. Thank you for your help, your friendship, your cheer, and your invaluable advice during my graduate orientation/visiting weekend.

Thank you to Professor Franz Kaertner for his numerous advice, and for giving me the opportunity to work on the EPHI project. Thank you to Janet Fischer for giving me the guidelines on the requirements of an MS thesis, for constantly providing graduate students with important academic and social information, and for giving me multiple extensions on this thesis. Thank you to Professor Palacios for helping me with my class choices and making sure I stay on track academically. Thank you to Donna L. Gale and to Dorothy A. Fleischer, for helping to maintain OQE group operating smoothly. Thank you to Professor M. R. Watts and to Ami Yaacobi for giving me the opportunity to work on nanoantennae project. Thank you to Katherine L. Hall for being my female mentor, and for providing numerous advice/encouragement on my way to finishing up this thesis.

Thank to my numerous collegeus here in the OQE group, some already Doctors, some soon to be: Michelle Sander, Michael Peng, Hang-Wen Chen, David Chao, Ben Potsaid, Cheri Sorace, Patrick Callahan, Jonathan Cox. Thank you for your friendship and for stimualting scientific discussions that we have in the offices/labs/hallways.

Thank you to all my friends, especially Ahmed Helal, Katherine Ruiz, and Jonathan Morse, for helping me, listening to me, and laughing with me on occasion. Your friendship is truly invaluable.

Jonathan Morse deserves a special thank you reserved just for him. Thank you for all your help building and machining optical mounts for my projects, thank you for being very well organized with your lab supplies, to the point where I could always find what I needed in your lab if I could not get it in my own, thank you for helping me with my TQEs, thank you for letting me borrow your car on numerous occasions, thank you for being a fantastic friend, and a much-needed office-mate. I am very lucky that I've got you as an office-mate, and I hope our friendship will continue for many years after you graduate.

Thank you to the professors I worked with at my undergraduate insitution (College of Optical Sciences at the University of Arizona), Robert A. Norwood, and Franco Kueppers. I would have never gotten into MIT if it were not for your help and guidance. I will never forget it. Thank you.

Thank you to my dear, loving, beautiful family: my mom, my dad, my three sisters (Tania, Aleks, Anastasia) and my brother Evan. Your love and support guide me through every day. I am a lucky person to have so many people who truly love me.

And finally, thank you to my dear son Daniel, for making me the happiest woman alive, for making my days, my smiles, my neverending desire to move forward. I love my lab and my research, but there has never been a day when I was not looking forward to coming home finally after a long work day, to see you, and to spend another priceless evening with you. I love you every day.

Contents

List of Figures

List of Tables

Chapter 1

Introduction

1.1 Photonic Integrated Circuits / Silicon Photonics

In the last few decades there has been a considerable interest and effort among the scientific community to develop photonic integrated circuits (PIC), which include several all-optical components on the same chip. Often, such all-optical components are integrated with electronic ones in what is called electronic-photonic integrated circuits (EPIC). Transition towards more optical components as opposed to electronic ones allows for a more compact system, with better performance, higher functionality, and significantly reduced electrical power dependance. All-optical devices that could potentially be made on a chip include lasers, detectors, interconnect waveguides (including couplers, power splitters/combiners), optical amplifiers and modulators, and filters [3, 4]. While there have been several established platforms for fabricating such devices, the silicon-on-insulator SOI platform emerged recently as one of the more promising candidates for all-optical integration. SOI systems have been recently demonstrated to perform all-optical switching, modulation, and analog-to-digital conversion at optical C-band wavelengths (1530-1565 nm) [5, 6, 7]. The advan-

tage of the SOI platform is that it provides the high index-contrast necessary for the strong light confinement, which, along with nanoscale dimensions, allows for high-intensity single mode operation of a device. In addition, silicon-on-insulator systems can be fabricated using state-of-the art complimentary metal-oxide semiconductor (CMOS) fabrication process, originally developed for electronics, which by now has become an industry standard. Still, while SOI systems have been leading the electronic-photonic circuits research, two of the known bottlenecks of using silicon for optical waveguides are its indirect energy gap, which makes it hard to make all-optical silicon laser, and its strong two-photon absorption at communications C-band wavelengths.

While silicon has a lot of advantages as a leading material for all-optical circuits (such as low loss around $1.5\mu m$, the index of refraction around 3.5, and high nonlinear susceptibility), its bandgap is 1.1 eV at room temperature, which supports two-photon absorption for wavelengths below 2.26μm. At high powers, the effects of this two-photon absorption and two-photon-absorption-generated free carrier absorption lead to a non-desirable non-linear loss, and limitations to the nonlinear phenomena. These effects have been widely studied and analyzed in the literature [8, 9, 2]. Therefore, there has been a considerable interest in alternative materials that could potentially be used in place of silicon and that would not be limited by two-photon absorption. In this thesis, we introduce polycrystalline anatase TiO_2 as one such novel material.

1.2 Titanium Dioxide: An Introduction

Titanium dioxide is a common industrial material that most often comes in the form of white powder and which, due to its high refractive index and brightness, has been widely used as a white pigment. In fact, titanium dioxide is one of the most commonly used pigments in

everyday items like medicines (pills), paints, plastics and coatings [10]. Additionally, TiO_2 has strong UV absorption, and thus has been used in numerous sunblocks.

TiO_2 exists in three different crystalline phases: brookite(orthorhombic), rulite(tetragonal), and anatase(tetragonal). The brookite phase has proven to be most difficult to fabricate, and thus it has not been as thouroughly investigated as the rutile and anatase phases [11]. Rutile is the most commonly occurring in nature and the one most easily fabricated, while anatase phase can be stabilized at higher temperatures. The anatase form of TiO_2 has been long known to be a strong photocatalyst under UV light. As such, titanium dioxide has been addcd to the numerous compounds, such as cements, paints, and various liquids as a hydrolysis catalyst [12, 13].

In addition to its pigment and photocatalysis use, titanium dioxide has found applications in photovoltaic research. Several types of solar cells incorporate TiO_2 as one of their thin film layers. One such example is a dye-sensitized solar cell (DSC), which is based on low-cost materials (unlike silicon-based photovolatics), with cell efficiencies reported to be 11-12%. In such solar cells, a nanocrystalline metal-oxide film (often TiO_2) is deposited onto a conducting substrate, which is sensitized to visible light using a photo dye [14]. In addition to DSCs, TiO_2 has been used as a semiconductor acceptor material in bulk heterojunction organic solar cells, where the electron donor is a certain semiconductor polymer, and an acceptor is a semiconductor metal oxide [15]. Such solar cells, although still having relatively low efficiencies, have been very useful in studying exciton dynamics. Due to its high refractive index, TiO_2 has also been used in Bragg mirrors as an anti-reflection coating material [16].

Recently, titanium dioxide has also attracted attention as a photonic material that has the potential for low loss light propagation at 0.8 and 1.5 μm [17, 1] and high electronic

bandgap that does not support two-photon absorption in the C-band wavelength range, and has low two-photon absorption around 800nm [18]. Thin films of both rutile and polycrystalline anatase have been demonstrated previously, with nonlinear indices at 800nm reported to be significantly larger then those of silica [19, 20]. While non-linear optical properties of anatase at 800nm have been studied in thin films, previous work does not include non-linear characterization of anatase TiO_2 nanowaveguides around 1550nm. This work focuses on polycrystalline anatase TiO_2 nanowaveguides and their non-linear optical properties around 1550 nm, and establishes polycrystalline anatase TiO_2 as an alternative to silicon in photonic-integrated circuits.

1.3 Thesis Overview

This thesis is organized as follows: Chapter 2 describes the structure and fabrication of the proposed polycrystalline TiO_2 devices, provides some basic characterization and SEM images, and lists some basic optical parameters. Chapter 3 describes spectral broadening measurements, the detailed experimental setup and the analysis. Estimates of the third order nonlinearities determined from those measurements are given at the end of the chapter. Chapter 4 describes the heterodyne pump-probe technique, the theory and numerous experimental details. The chapter continues with presenting unprocessed heterodyne pump probe data, the procedure to extract the nonlinear parameters from these data, and the resulting estimates of the third order nonlinearities. Chapter 5 summarizes the work done, and provides a discussion on the future work and the potential of the TiO_2 waveguide devices.

Chapter 2

Anatase TiO_2 Waveguides

2.1 Fabrication

The polycrystalline anatase TiO_2 waveguides presented in this thesis were fabricated by E. Mazur's group [21, 1] at Harvard University, Cambridge, MA. The waveguides were deposited using reactive radio frequency magnetron sputtering of titanium, using oxygen flow of 4.4-20 sccm, at 350° C, with the pressure of 2mTorr [1]. The thickness of the deposited film was measured to be 250 nm. Raman spectroscopy was performed on the films made on glass substrates in order to confirm the resulting crystalline phase as polycrystalline anatase [22]. The spectrum is shown in Figure 2-1, which confirms characteristic anatase Raman shift of 141 cm^{-1}. Figure 2-2 shows a scanning electron microscope (SEM) image of the film. The ridge waveguide geometry was structured using standard top-down e-beam lithography followed by TiO_2 film deposition on top of the SiO_2 layer on a silicon substrate. Cytop^{TM} polymer was used as a low-index top-cladding layer. The dimensions and structure of the waveguides are shown in Figure 2-3. Several waveguide geometries have been fabricated in order to manage dispersion and establish the single mode operation for various

wavelengths. Table 2.1 shows waveguide parameters for the four different waveguides.

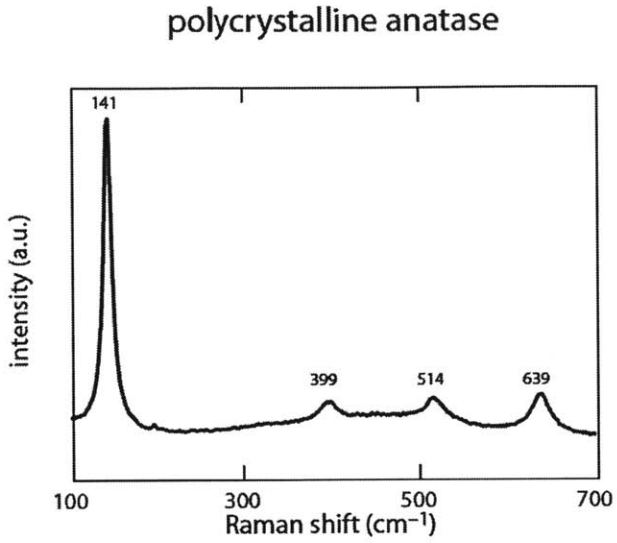

Figure 2-1: Raman spectroscopy data of the polycrystalline anatase TiO_2 film. Image courtesy of C. Evans [1].

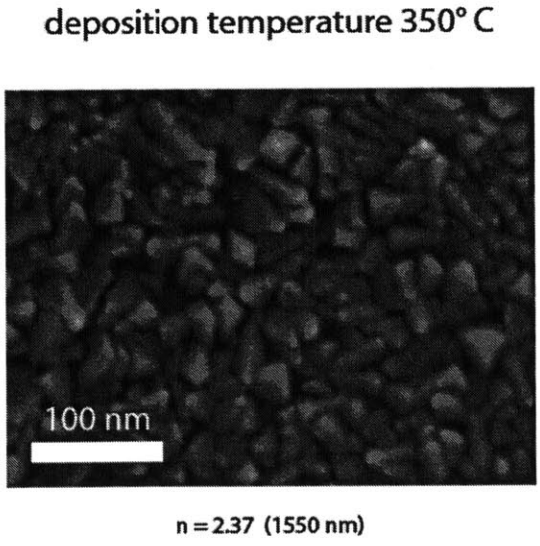

Figure 2-2: SEM image of the polycrystalline anatase TiO_2 film. Image courtesy of C. Evans [1].

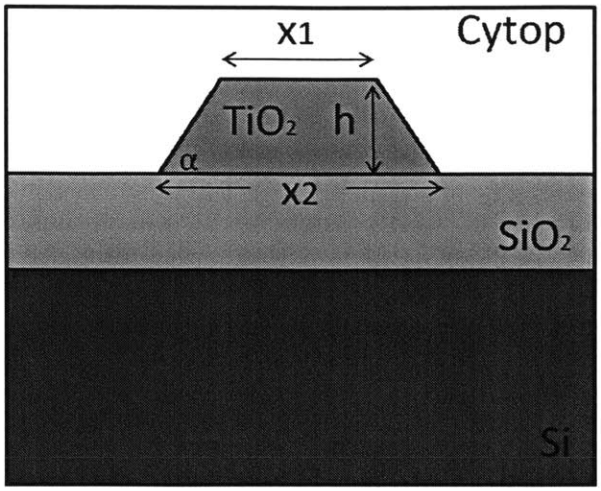

Figure 2-3: Structure/geometry of the fabricated TiO_2 waveguides.

Name	x_1	x_2	h	α
	nm	nm	nm	°
Waveguide 4	900	718	250	70
Waveguide 3	800	618	250	70
Waveguide 2	700	518	250	70
Waveguide 1	600	418	250	70

Table 2.1: Fabricated waveguide parameters

2.2 Optical Parameters / Characterization

The electronic bandgap of anatase TiO_2 material is 3.1 eV. This restricts TPA to λ <800nm. Refractive index measured by the prism-coupling method is n(1550nm)=2.37. The physical length of each waveguide is 9.2mm.

All the waveguides were designed to support only TE mode, and are therefore polarization sensitive. The TE mode profile of waveguide #3, which was used for both heterodyne pump-probe and spectral broadening measurements, is shown in Figure 2-4. Simulated dispersion values (D parameter) for waveguide #3 are shown in Figure 2-5, indicating normal dispersion.

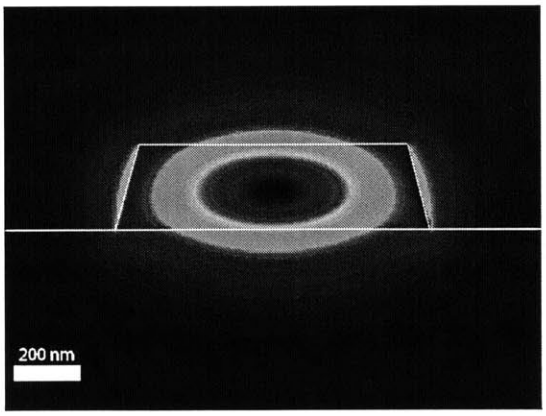

Figure 2-4: TE mode profile for waveguide #3. Image courtesy of C. Evans [1].

Linear optical propagation losses of the waveguides were measured using the top-view method [17, 23]. 1550 nm light was focused into the input facet of the waveguide using an optical objective (60x), with a half-wave plate and polarization beam cube preceding the objective in order to control the input polarization state. Top-view images were captured by an InGaAs camera with a linear polarizer in front of it to get rid of the light scattered by the input facet. By stitching such top-view images along the device and measuring relative

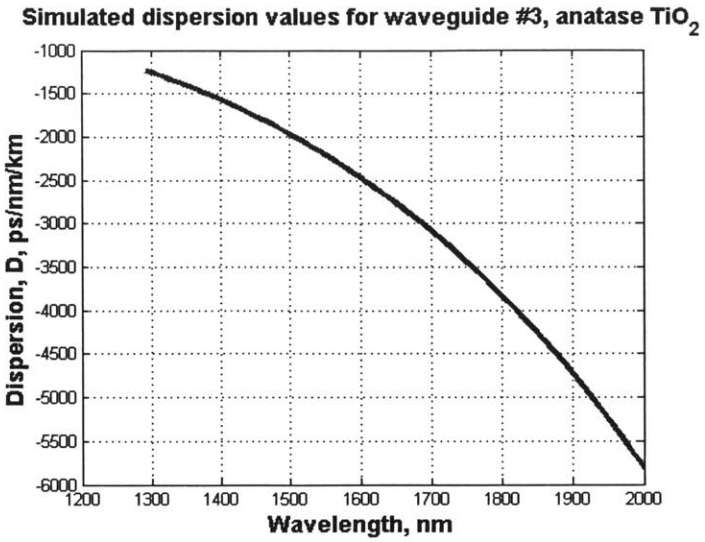

Figure 2-5: Simulated dispersion values for waveguide #3.

intensity of the scattered light, linear losses were determined to be ~7dB/cm. Examples of the top-view images taken are shown in Figure 2-6.

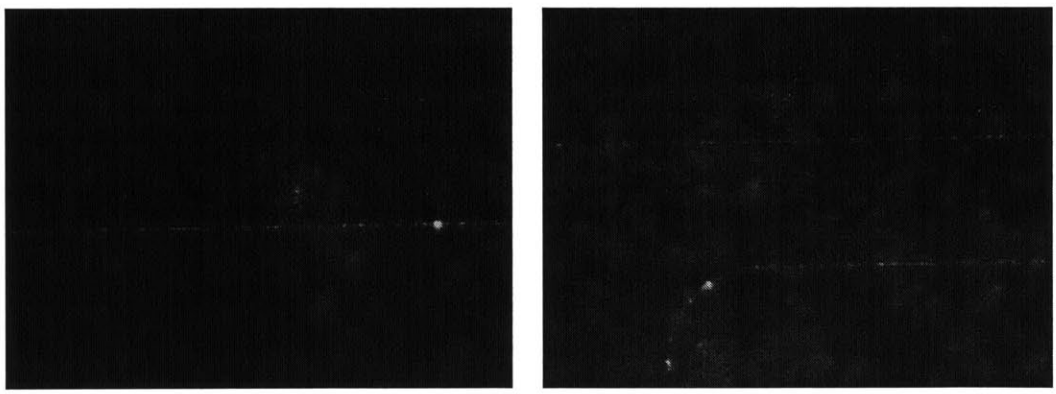

Figure 2-6: Top view linear loss images

Chapter 3

Spectral Broadening Measurements

3.1 Theory

Spectral broadening experiments are based on the self-phase modulation (SPM) nonlinear optical effect, which is in turn based on optical Kerr effect. When an ultrafast optical pulse propagates through a nonlinear medium, it introduces intensity-dependent refractive index changes, which in turn modulate the phase and the frequency spectrum of the optical pulse. Intensity-dependent refractive index can be described according to Equation 3.1, where n_0 is the linear refractive index, and Δn is the intensity-dependent part, I is the light intensity inside the medium, and n_2 is a second-order nonlinear refractive index coefficient, also called the optical Kerr coefficient.

$$n = n_0 + \Delta n = n_0 + n_2 I \tag{3.1}$$

This intensity-dependent refractive index introduces an intensity-dependent optical phase

delay in the pulse, which, at any given time t can be written as

$$\Delta\phi = \frac{2\pi}{\lambda_0} L\Delta n = \frac{2\pi}{\lambda_0} L n_2 I \tag{3.2}$$

where λ_0 is the central wavelength of the pulse, and L is the propagation distance. Corresponding instantaneous frequency change is given by Equation 3.3:

$$\Delta\omega(t) = -\frac{d(\Delta\phi)}{dt} = -\frac{2\pi}{\lambda_0} L n_2 \frac{dI}{dt} \tag{3.3}$$

This instantaneous frequency change is dependent on the time-dependent pulse intensity. For positive n_2, increasing intensity produces a shift to lower frequency, and decreasing intensity produces a shift towards higher frequency. The more rapid the changes in the intensity, the greater the frequency shifts. This concept is illustrated in Figure 3-1. The top plot shows normalized pulse intensity, for a $sech^2$ shape pulse with pulse duration τ_p=200 fs, given by $I(t) = I_0 sech^2(t/\tau_p)$. The change in instantaneous optical phase for such a pulse is given by Equation 3.2, and is plotted in normalized units, such that $k_0 n_2 L = 1/I_0$, which gives $\Delta\phi = k_0 n_2 L I(t) = sech^2(\frac{t}{\tau_p})$. Change in instantaneous frequency, given by Equation 3.3, for $sech^2$ pulse becomes $\Delta\omega = -\frac{dI}{dt} = -\frac{d}{dt}(sech^2(\frac{t}{\tau_p})) = \frac{2}{\tau_p} sech^2(\frac{t}{\tau_p}) tanh(\frac{t}{\tau_p})$, and is shown at the bottom plot in Figure 3-1.

This non-linear frequency change results in the broadening of the pulse spectrum, with higher n_2 values resulting in higher broadening. Figure 3-2 shows a simulation of SPM effects on the spectrum of a $sech^2$ pulse, with dispersion set to zero, and pulse duration of 200 fs. The following parameters were used: $n_2 = 10^{-15} cm^2/W$, $\gamma = 10^{-8} cm/W$, $\alpha = 8dB/cm$, $L_{eff} = 5mm$, $\lambda_0 = 1550nm$, $A_{eff} = 3 \times 10^{-9} cm^2$, R=80 MHz, and $\tau_p = 200fs$. Table 3.1 shows the peak pulse intensity, pulse energy, and corresponding phase shifts for the

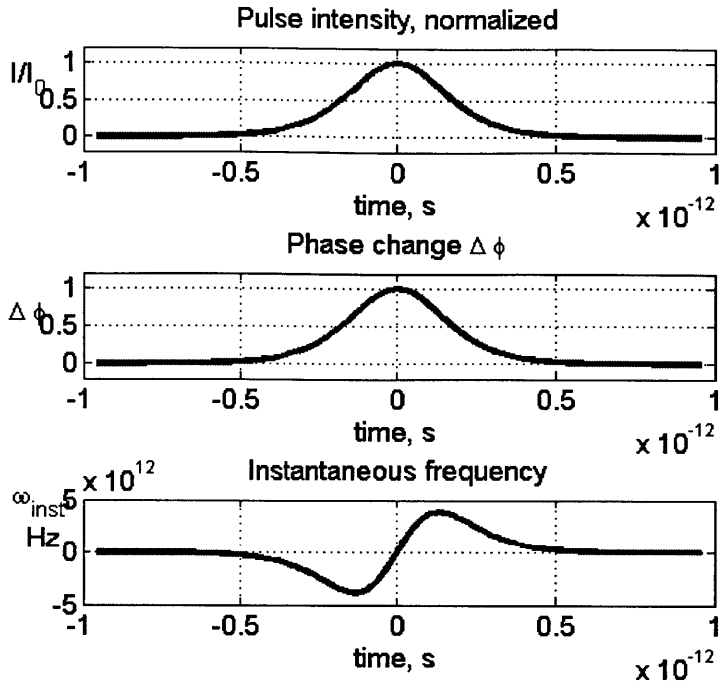

Figure 3-1: Self-phase modulation effects on $sech^2$ pulse, with τ_p=200 fs. Top plot - pulse intensity; middle plot - phase change due to optical Kerr effect; bottom plot - instantaneous frequency change.

four shown plots. By measuring this broadening of the spectrum of a known optical pulse propagating through a device, it is possible to estimate the peak phase change responsible for such broadening, which allows the optical Kerr coefficient to be calculated from the phase change.

Peak Intensity I_0	Pulse energy	Phase shift
$10^9 cm^2/W$	pJ	rad
0.3138	0.2139	$\pi/2$
0.6275	0.4279	π
0.9413	0.6418	$3\pi/2$
1.2551	0.8557	2π

Table 3.1: Peak pulse intensity and energy for SPM-induced phase shift, simulated parameters

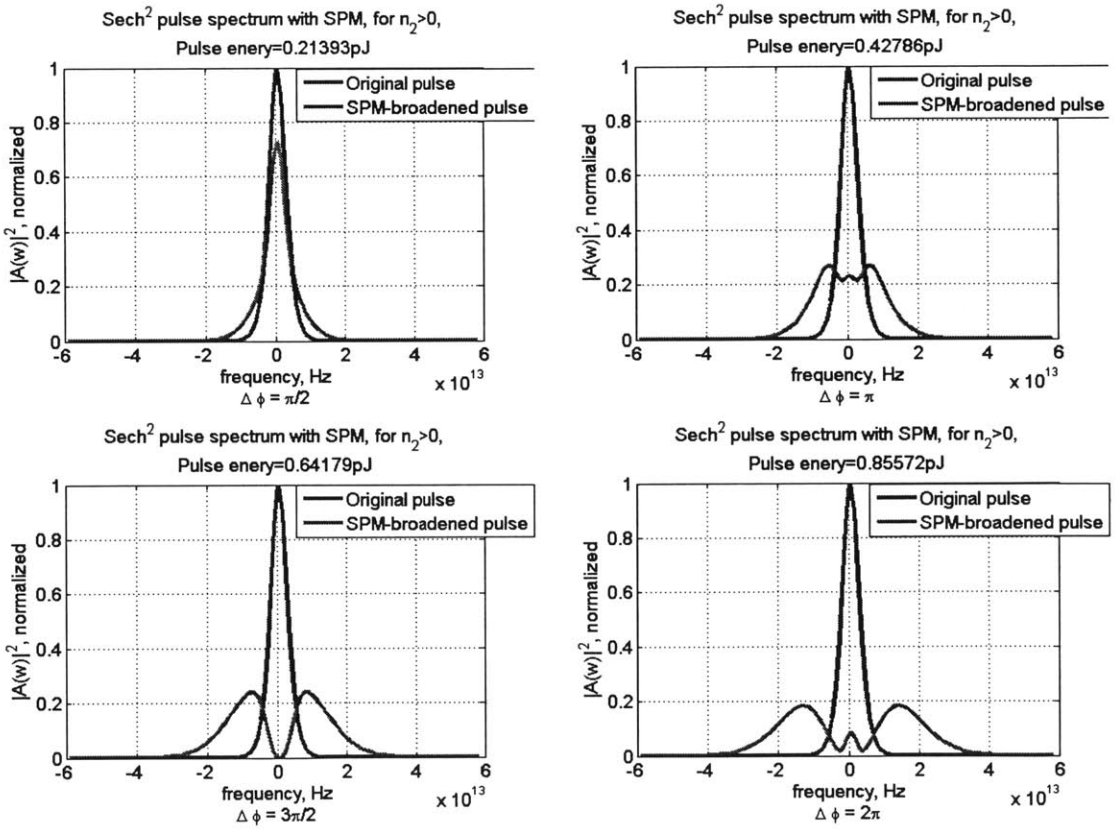

Figure 3-2: Spectral broadening simulations as a result of self-phase modulation, with zero dispersion.

3.2 Experimental Setup

The experimental setup used for spectral broadening studies is shown in Figure 3-3. The laser used for the experiment is a Spectra Physics Opal, synchronously pumped, optical parametric oscillator (OPO) pumped by a *MaiTai* titanium sapphire laser system. For this experiment, the pulse repetition rate was 80 MHz, and the wavelength was centered at 1565nm. The pulse full-width-at-half-maximum (FWHM) width was measured to be 173.7 fs. In the experiment, the optical beam from the laser is directed through a half-waveplate and a polarizing beam splitter (PBS) cube into the 0.85 NA 60x microscope objective that couples the light into the waveguide. The waveguides used in this work only support single polarization; therefore, the PBS is used in transmission such that TE mode enters the waveguide. Another identical objective collects the light at the output of the waveguide and directs it into either the power meter, or optical spectrum analyzer (OSA), depending on the position of the flip-mounted mirror. The power of the incoming light was varied using the waveplate in front of the polarizing beam splitter cube. Optical power was measured both before the input objective and after the output objective for each measurement.

Since spectral broadening and nonlinear refractive index are functions of the optical power inside the waveguide, it is necessary to properly characterize coupling losses. Coupling losses were calculated assuming the losses at input and output facets were identical. At low power levels, we can assume losses due to nonlinearities to be zero. Therefore, power measured at the output of the waveguide is a linear function of the input power, and can be written according to Equation 4.6, where P_{out} and P_{in} are input and output powers in dBm, C_1 is the coupling loss at either input or output facet, α is linear loss in dB/cm, and L is the physical length of the device. For the waveguide used in the spectral broadening experiment, $\alpha = 8dB/cm$, and L=9.2 mm, which results in a total linear loss of 7.36 dB.

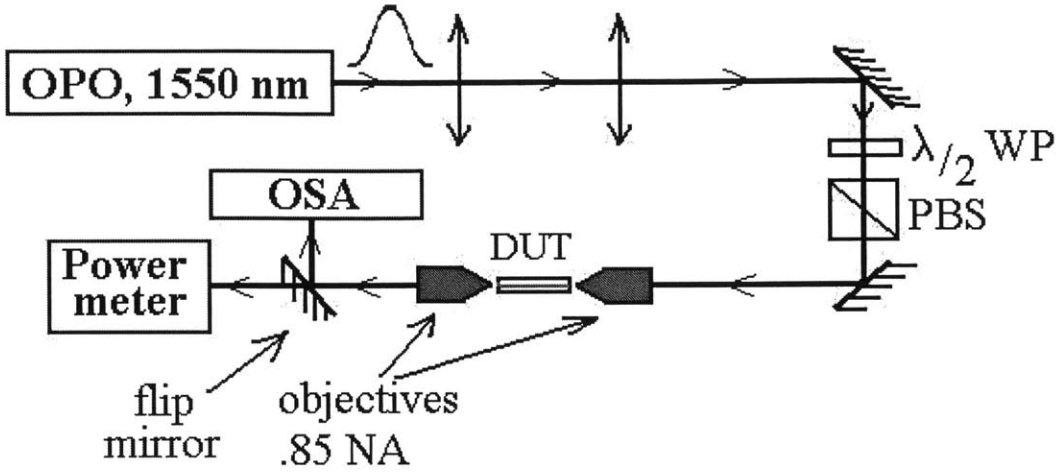

Figure 3-3: Experimental setup for SPM measurements.

$$P_{out} = P_{in} - 2C_1 - \alpha L \tag{3.4}$$

Measured output power is plotted versus input power in Figure 3-4 (a), which ideally should be a linear plot. We assume that any deviations from a perfect line in this plot are due to optical misalignment of the input. Coupling loss C_1, calculated from Equation 4.6, is shown in Figure 3-4 (b) vs input optical power. In this Figure, any deviations from a constant C_1 value are most likely due to input optical misalignment, therefore, we take the lowest value of $C_1 = 11dB$ as the actual input coupling loss, which corresponds to the best alignment.

The optical spectrum of the OPO, prior to passing through the TiO_2 waveguide, is shown in Figure 3-5, for a measured pulse width of 173.7 fs.

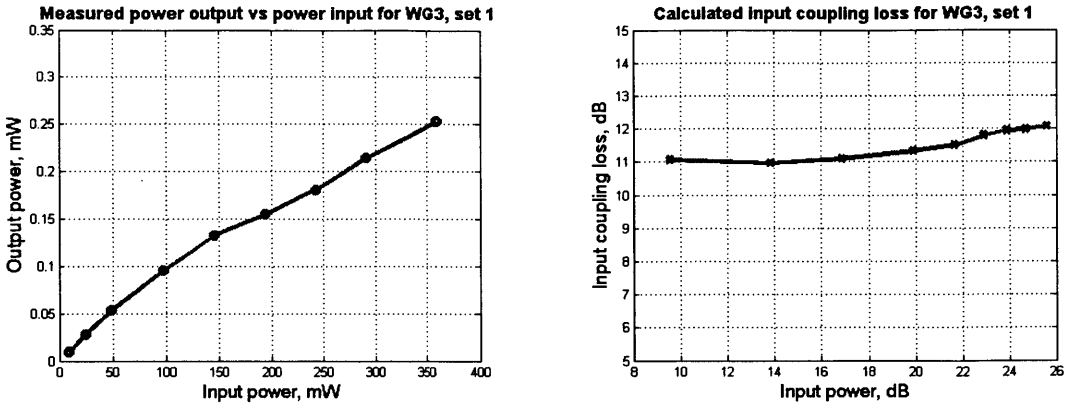

(a) (b)

Figure 3-4: Coupling Losses: (a) measured output power vs input power, (b) calculated coupling losses vs input power

3.3 Results / Analysis

3.3.1 Spectral broadening results

Figures 3-6 and 3-7 show unprocessed broadened spectra as measured by OSA using the setup shown in Figure 3-3. The plots are not normalized, and are shown in the order of increased optical power, with Figure 3-7 showing significantly broadened spectra. Spectral broadening is not easily visible until the pulse energy reaches ~80 pJ (Figure 3-6, (c)). Figure 3-7 shows significant strong spectral broadening at pulse energies of 200-300 pJ. We note the general differences between Figures 3-6 and 3-7, which show measured data, and Figure 3-2 that shows simulated data. One of the differences is that the simulated plots did not include dispersion, which is present in real devices. Estimated dispersion value for measured device is D=-2000ps/nm km, which corresponds to normal dispersion and will, therefore, add to the effects of the self-phase modulation by broadening the pulse. The second difference is the apparent asymmetry of the measured broadened spectra at higher powers. This is most evident in Figure 3-7 with both plots exhibiting an extra peak on

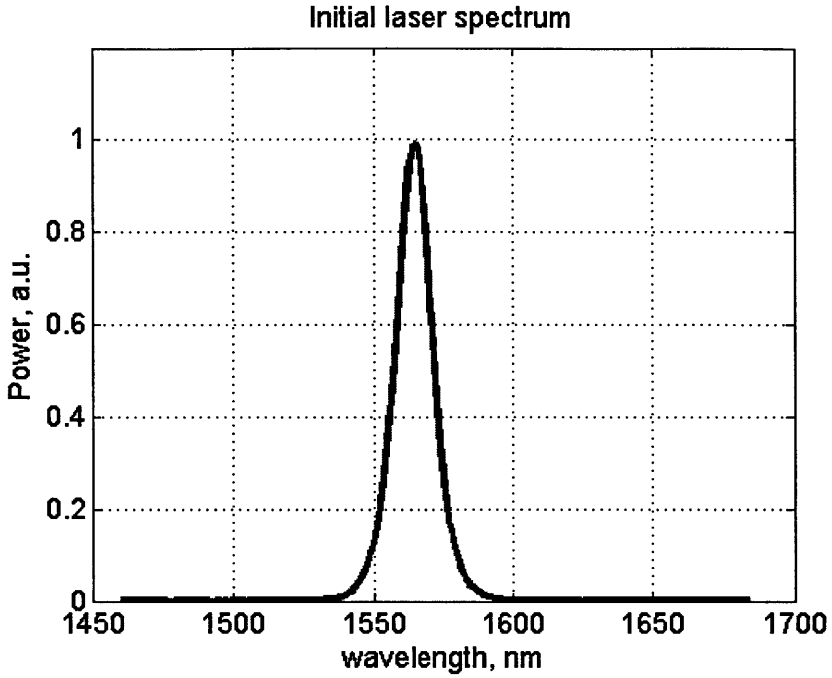

Figure 3-5: Measured spectrum of OPAL OPO with τ_p=173.7 fs.

the right hand side of the spectrum. The peak becomes more distinguished at higher pulse energies and appears to shift towards higher wavelengths. We attribute this asymmetry to stimulated Raman scattering in the material. Section 2.1 presented an overview of material properties for anatase form of TiO_2 , with the Raman spectrum shown in Figure 2-1. The Raman structure that is responsible for asymmetry of our spectral broadening measurements occurs at $\nu = 141cm^{-1}$. In general, Raman frequency is given by Equation 3.5, where λ_0 is the excitation wavelength, and λ_R is the observed Raman wavelength. Using λ_0=1565nm as the central wavelength and $\nu = 141cm^{-1}$, λ_R is calculated to be $1.6\mu m$. Such Raman peak at $1.6\mu m$ starts to become noticeable in Figure 3-6, (c), where the spectrum begins to look asymmetric. At higher pulse energies, the superposition of the spectral broadening of the initial pulse and that of the Raman line causes the Raman peak to move towards

higher wavelengths, and the spectrum to look even more asymmetric.

$$\nu = \frac{1}{\lambda_0} - \frac{1}{\lambda_R} \tag{3.5}$$

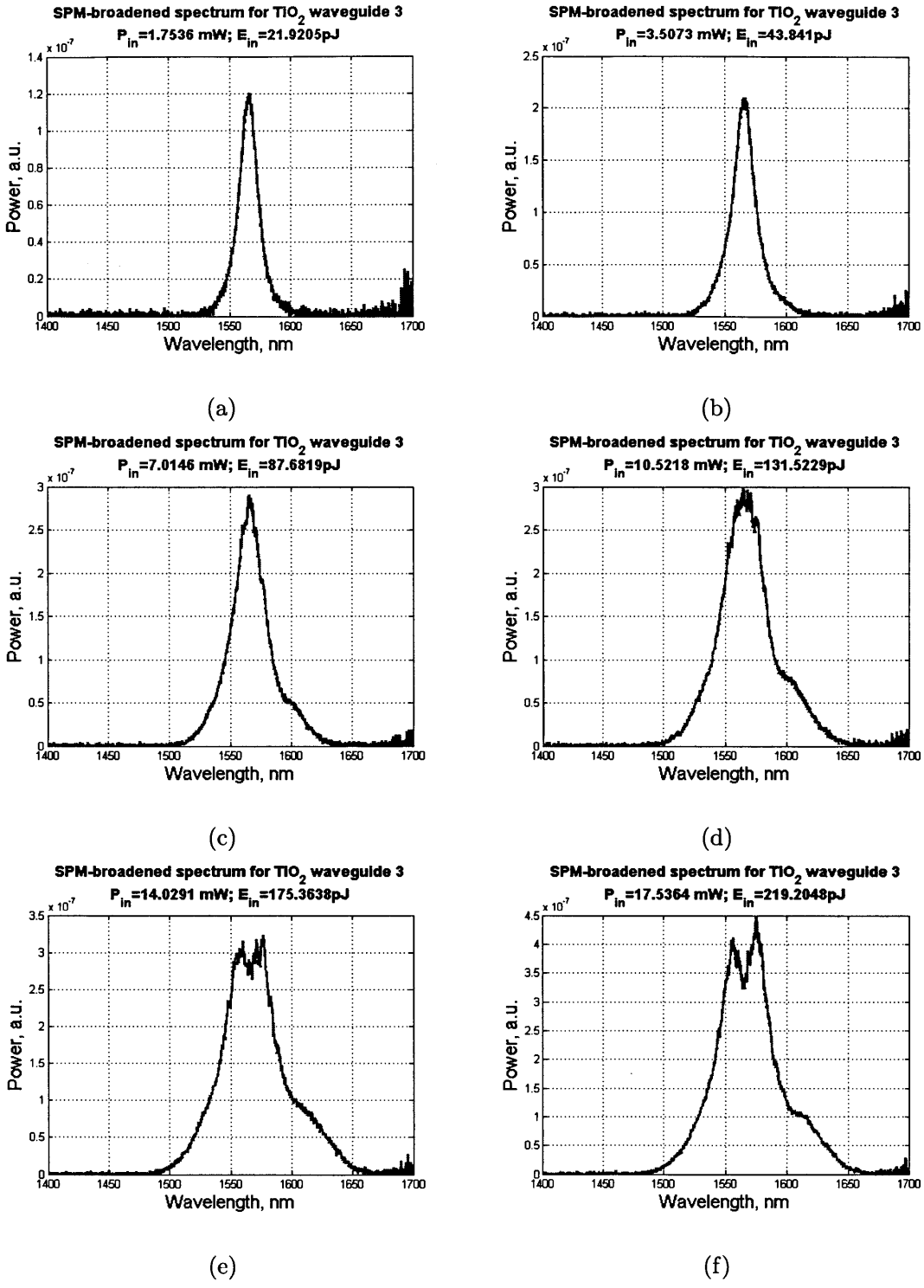

Figure 3-6: Unprocessed SPM spectrum measurements for TiO_2 waveguide #3.

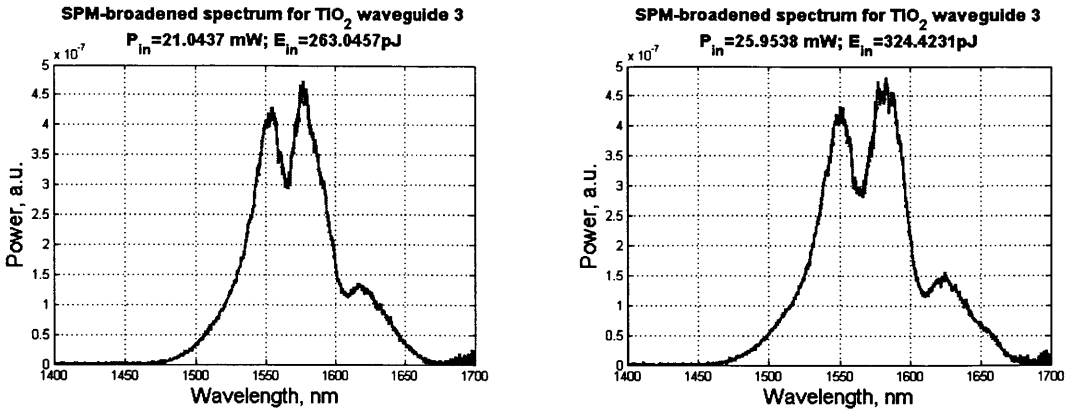

(a) (b)

Figure 3-7: Unprocessed SPM spectrum measurements for TiO_2 waveguide #3.

The effects of the Raman shift and dispersion both need to be considered when trying to extract nonlinearity values from measured plots. RP Fiber Power software, that models several linear and nonlinear processes simultaneously, was used to do the analytical fitting in order to determine the correct SPM-induced phase shift. Table 3.3.1 shows the final parameters used for this fitting model, and Figure 3-8 shows fitted results superimposed on the measured results. The nonlinear refractive index n_2 that resulted in good analytic fits that match measured data was determined to be $1.82 \times 10^{-15} cm^2/W$, which, with femtosecond pulses with energy E=229pJ, results in the phase shift of $\Delta\phi = 1.5\pi$. In comparison, the well-established value of n_2 for silica glass in SMF fiber is $\sim 2.79 \times 10^{-16} cm^2/W$ [24, 25]; the well-established value of n_2 for silicon ranges from 4 to 6 $\times 10^{-14} cm^2/W$ [26, 27, 28, 29]; the well-established value of n_2 for silicon nitride is $\sim 2.4 \times 10^{-15} cm^2/W$ [30]. Polycrystalline anatase TiO_2 waveguide therefore allows for a nonlinear refractive index that is an order of magnitude higher than that of silica glass, and comparable to silicon nitride, which makes TiO_2 a good candidate for nonlinear optical applications.

Pulse width	τ_0	167.3	fs
Central wavelength	λ_0	1565	nm
Group Delay Dispersion for input pulse	GDD	36×10^{-3}	fs^2
Nonlinear refractive index	n_2	1.82×10^{-15}	cm^2/W
Two-photon absorption	β	0	cm/GW
Delayed Raman value	τ_1	33.25	fs
Raman line width	τ_2	2.2×10^3	fs
Delayed Raman fraction	f_R	0.285	
Linear loss	α	7.975	dB/cm

Table 3.2: Parameters used in analytical fitting model for SPM process with dispersion and Raman shift

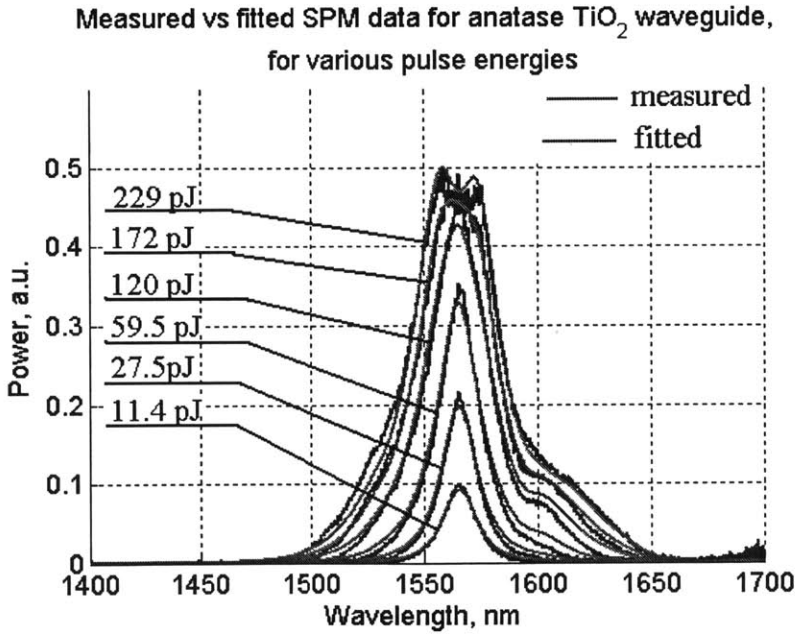

Figure 3-8: Analytical fits to measured data for spectral broadening in anatase.

3.3.2 Third Harmonic Generation in TiO_2 waveguides

During spectral broadening experiments, at higher pulse energies, a bright green light emission was noticed, appearing from the top surface of all the waveguides measured. The brightness of this green up-emission increases the with input pulse energies; and the color shifts towards bluer wavelengths when the input wavelength is shortened. In this section the investigation of this phenomenon is presented, and the up-emitted green light is attributed to the third harmonic of the fundamental wavelength. Figure 3-9 (a) shows the image of the waveguide and the two objectives in the visible light, with a bright green emission clearly visible on the right hand side of the waveguide. A top view image of this waveguide, with visible green light emission, is shown in Figure 3-9 (b). This image was taken with a black-and-white CCD camera, with a zoom lens attached to it, located exactly above the waveguide; therefore, what is visible as a white light emitted from the waveguide, is actually green, similar to that in part (a) of the Figure.

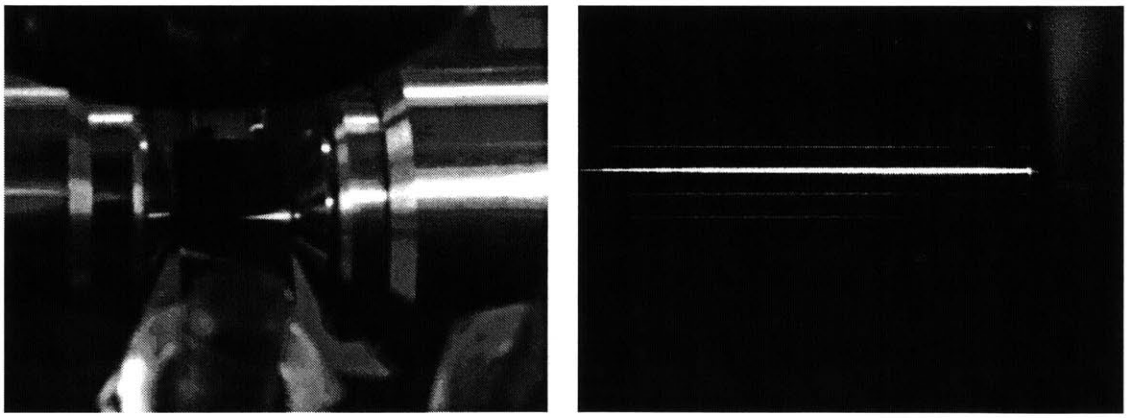

(a) (b)

Figure 3-9: (a) Green up-emission from TiO_2 waveguide #4, with input power of $\sim$ 300mW; (b) Top view image of the up-emitted light (green), taken with black-and-white CCD camera.

The spectrum of this up-emitted light was taken with a scanning multimode fiber

mounted such that it collected the light from the top surface of the waveguide, with the light from this multimode fiber going into OceanOptics spectrometer. We note that the setup was aligned for 1550 nm. Therefore, with significant wavelength tuning away from 1550 nm, the input power into the waveguide decreased due to slight optical misalignments that resulted from the wavelength change, and the coupling loss between the input objective and the waveguide increased. Normalized green light spectra, measured for three different input wavelengths (1500nm, 1550 nm, and 1581 nm) are shown in Figure 3-10. For 1500nm and 1550 nm fundamental wavelengths, measured up-emitted spectra peak at 500nm and 517nm respectively, which precisely corresponds the third harmonic of their respective fundamental wavelengths. For 1581 nm fundamental wavelength, the green line spectrum peaks at 524nm, which is 3 nm below the exact third harmonic of 1581nm. We attribute this to the instability of the laser at 1581nm, and the interference within the multimode fiber. The change in tilt, the angle, or the position of the multimode fiber was noticed to shift the peak wavelength by a few nanometers. The spectrum for 1500nm appears very noisy. This is due the fact that, at 1500 nm, the up-emitted light intensity was significantly lower due to increased coupling losses into the waveguide. All three spectra in Figure 3-10 are normalized, such that the peak power for each input wavelength appears to be the same.

Figure 3-11 shows third harmonic light intensity as a function of length along the waveguide for various pulse energies, plotted on the log-y scale. The plots were obtained by analyzing top-view images similar to the one shown in Figure 3-9 (b) for various input powers at 1550 nm. THG intensity was calculated by summing the pixels of a fixed bucket size along the waveguide. The plots for the pulse energies above 90 pJ clearly saturated the CCD array, which is evident in plots being on top of each other, despite having significantly higher input pulse energies. Figure 3-12 shows the THG intensity (obtained by analyzing top view

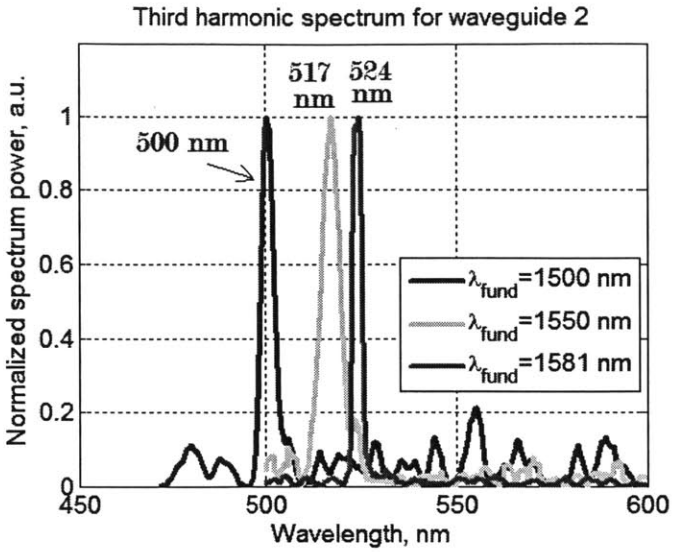

Figure 3-10: Spectrum of the third harmonic lines for waveguide #2, for three input wavelength values.

images) at some fixed point along the waveguide, vs input pulse power. Also shown is the fit, which is proportional to the input optical power to the 3^{rd} power. Third order nonlinear polarization that is responsible for the third harmonic generation is proportional to $\chi^{(3)}|E^3(\omega)|$, where $\chi^{(3)}$ is the third order nonlinear susceptibility, and $E(\omega)$ is the incoming electric field at the fundamental wavelength. The power generated at the third harmonic is in turn proportional to the intensity at the fundamental wavelength cubed. The fit is in a good agreement with experimental data for low input powers, corresponding to pulse energies under 50 pJ. For higher values, THG intensity is significantly lower than predicted. Among the reasons responsible for this intensity drop are the apparent saturation of the CCD camera used to take the images for this analysis, and possibly pump depletion.

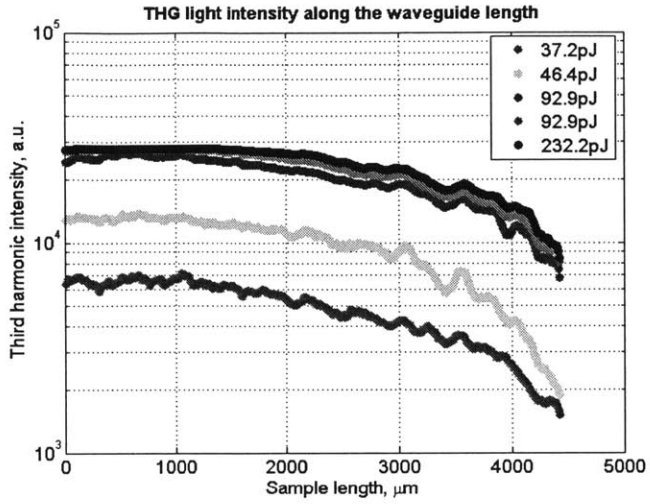

Figure 3-11: Third harmonic up-emitted power (in a.u.) as a function of waveguide length, for various input pulse energies.

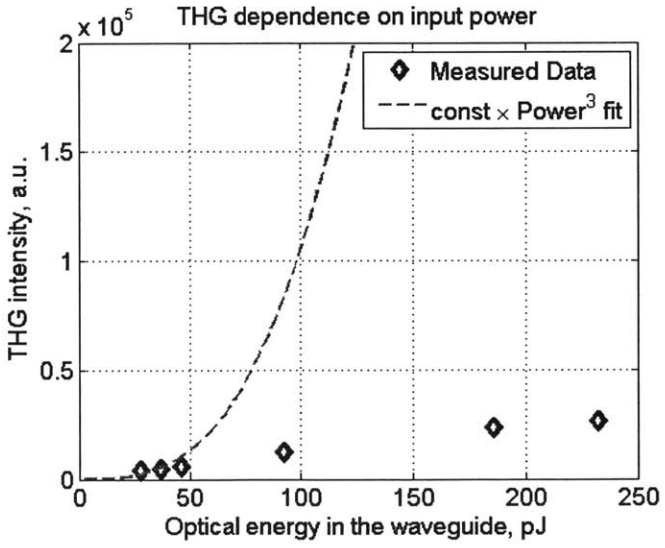

Figure 3-12: Third harmonic power vs input pulse energy at fundamental wavelength of 1550nm.

Chapter 4

Heterodyne Pump Probe Measurements

4.1 Theory

4.1.1 Pump-probe experiments

Femtosecond pump probe spectroscopy is a technique that allows for time-resolved studies of nonlinear dynamics in various materials devices [31, 32, 33, 34]. This technique involves exciting the device with a strong optical pulse (the pump), while monitoring the outcome of this excitation with a weaker pulse (the probe). By monitoring the change in the probe pulse as a function of time delay between the pump and the probe, it is possible to recover the nonlinear dynamics of various devices under study. Physical models of the device dynamics are then related to the pump-probe response curves in order to extract desired constants and parameters. By varying the intensity of the exciting pulse (the pump), the response of the device can be measured in both perturbational and highly nonlinear regimes. The resolution of such experiments is comparable to the cross-correlation of the pulses used.

Some of the material properties that could be extracted from pump-probe experiments are time-resolved absorption (a key measurement in characterizing saturable absorbers for mode-locked lasers), non-linear refractive index changes, dichroism and birefringence, non-linear absorption, and higher order nonlinearities. Depending on the desired parameters to be measured, and on the device structure, various pump-probe experiment configurations are used. In this work, degenerate pump-probe experiments are used, where the pump and the probe come from the same mode-locked laser beam. When the strong pump excites the material, and time-delayed probe is used to monitor pump-induced changes, there is a necessity to measure only the probe beam at the output of the device, as it will contain the material response due to pump excitation. Both the pump and the probe pulses are incident on the device with a femtosecond relative time delay, therefore, there exist various experimental techniques that measure the probe pulse only at the output of the device by separating it from the pump pulse. One common method of separating the pump and the probe is to have them orthogonally polarized with respect to each other prior to being incident on the sample. After the beams exit the device, a linear polarizer is used to pick only the probe polarization. A common schematic of such cross-polarized pump-probe experiment is shown in Figure 4-1.

In Figure 4-1, a mode-locked laser source is used to produce a train of optical pulses, which is separated into the pump and the probe beams by a polarizing beam splitter (PBS). The pump beam is time-delayed with respect with the probe beam by using a mechanical stage with high precision motion control, which translates along the direction of the beam. Time delay introduced into the beam is directly proportional to the distance the stage travels. After this time delay is introduced, the pump and the probe beams are recombined using another PBS, and are focused into the reflective sample. Yet another, third, polarizing

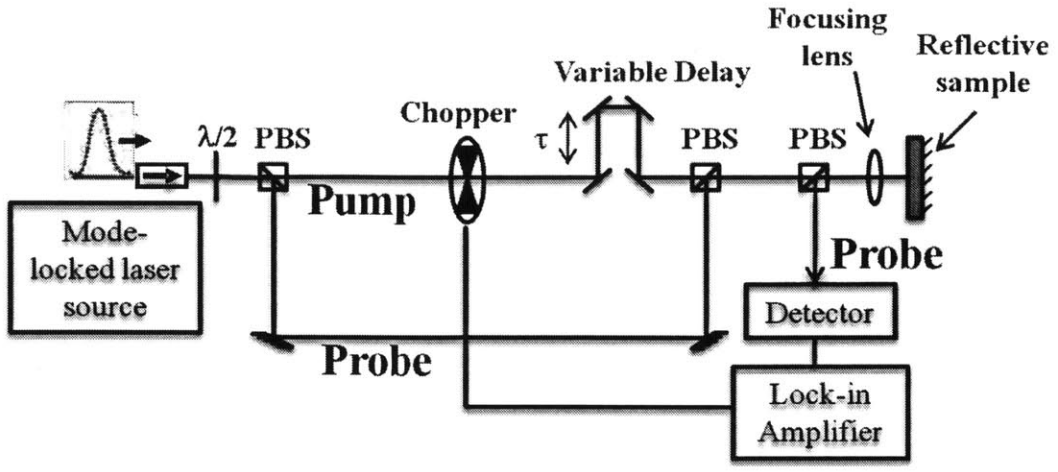

Figure 4-1: Degenerate cross-polarized pump-probe setup in reflection.

beam splitter cube is used in front of the sample to polarization-separate reflected beams as shown in Figure 4-1, and only the probe beam is detected. Usually the pump beam is chopped with a mechanical chopper, and the final signal is passed from the detector to a lock-in amplifier, which provides for background-free measurement. Since the probe beam is not being chopped, only the photons that interacted with the pump are detected after passing through the lock-in amplifier. This is a critical part of the experiment, which allows to measure changes in the sample properties due to the pump-induced excitation only. By adding extra half-waveplates into each of the paths, the intensities of the pump and the probe can be adjusted separately.

4.1.2 Heterodyne pump-probe technique

In order to measure the response of the system in pump-probe experiments, the probe beam needs to be separated from the pump, as mentioned in the previous section. This could be done spatially, spectrally, or by using cross-polarized beams. However, in certain experiments, none of those techniques lead to accurate results. One particular example is

measuring polarization-sensitive waveguides, where light propagation is highly dependent on the input polarization state. In such cases, the pump and the probe often need to be at the same wavelength, have the same polarization, and be confined in the same waveguide. In order to provide for an accurate measurement under such conditions, a new variation of pump-probe experiments called heterodyne technique was introduced in 1992 by Hall et al [35, 36]. This technique uses a small frequency shift to separate the pump and the probe, and uses a separate reference beam which beats with the probe signal on the photodetector. In such experiments, the train of probe pulses is being separated from the pump pulses by passing through a frequency-shifting element (usually an acousto-optic modulator (AOM)), which shifts the pulse train by a known frequency Ω_1, usually in an RF band. The pump pulse train is not shifted. A third, separate pulse train, termed a "reference" beam, which is initially taken from the same laser source as the pump and the probe beams, is also frequency shifted by a separate AOM by a known frequency Ω_2, such that the difference $\Omega_1 - \Omega_2$ can also be detected as an RF signal. The pump and the probe beams are made to overlap spatially and temporally in the waveguide being measured, with the pump beam having a variable controlled time delay, as described in Section 4.1.1. The reference beam does not pass through the sample, but is combined with the the pump/probe beams after they propagate through the waveguide. The reference beam is path-matched with the probe beam in order for the two beams to arrive simultaneously onto the fast photodetector. Under such conditions, the probe and the reference beams beat on the photodetector with a beat frequency equal to $\Omega_b = \Omega_1 - \Omega_2$. The polarization of the probe and the reference beams must be the same and thus a combination of a half-wave plate (HWP) and a quarter-wave plate (QWP) is placed in the reference beam path in order to adjust the reference beam polarization to a desired state. Usually, to obtain background-free measurements, the pump

beam is chopped using a mechanical chopper. The measured signal is demodulated using a radio receiver. The amplitude variation of the probe signal reflects the changes in pump-induced material absorption, and the phase variations of the demodulated probe signal reflect the phase changes induced in the sample.

The pump, the probe, and the reference beams can be represented as follows:

$$E_{pump} = Re\left\{E(t+\tau)c(t)e^{j\omega(t+\tau)}\right\} \tag{4.1}$$
$$E_{probe} = Re\left\{E(t)e^{j(\omega-\Omega_1)t}\right\}$$
$$E_{ref} = Re\left\{E(t)e^{j(\omega-\Omega_2)t}\right\}$$

In Equation 4.2, E_{pump}, E_{probe}, and E_{ref} are the electric fields of the pump, the probe, and the reference beams respectively. Ω_1 and Ω_2 are AOM-induced frequency shifts on the probe and the reference beams, τ is variable time delay, and c(t) is the chopping frequency. This representation ignores the polarization of the beams, and their relative amplitudes. The electric field at the input of the waveguide is the sum of the pump and the probe beams, and is written as:

$$E_{in} = E_{pump} + E_{probe} \tag{4.2}$$

The response of the heterodyne pump-probe experiment is the relative change in phase (for PM measurement) or in intensity (in AM measurement) of the probe beam. For simplicity, we will show the theory for the intensity measurement, however, the analysis of the material response presented in this section is identical for the phase measurement. The time derivative in a nonlinear change to material polarization P is written according to Equation

4.3, where h_{ijkl} is a tensor material response to the total input electric field polarization components E_j, E_k, and E_l. h_{ijkl} can be related to the third order nonlinear susceptibility $\chi^{(3)}_{ijkl}$.

$$\frac{\partial \Delta P_i}{\partial t} = \int dt'' E_j(t) h_{ijkl}(t - t'') E_k^*(t'') E_l(t'') \tag{4.3}$$

The change in optical intensity on the probe beam due to the pump beam can be written according to Equation 4.4, where d is a constant, and ΔP is the change in nonlinear pump-induced material polarization, given by Equation 4.3.

$$\Delta I = \frac{d}{2} \int dt Re \left\{ E^*_{probe} \cdot \frac{\partial \Delta P_i}{\partial t} \right\} \tag{4.4}$$

The quantity measured by a heterodyne pump-probe experiment is $\Delta I/I$ in AM mode (absorption change) or $\Delta\Phi/\Phi$ in PM mode (phase change).

4.1.3 Coherent Artifact

In order to get a full expression of the material response to the pump-probe input electric fields, Equations 4.2, 4.2, and 4.3 need to be substituted into Equation 4.4 with correct polarizations [37]. The result will consist of many terms, including pump-induced changes on the pump beam, probe-induced changes on the probe beam, probe-induced changes on the pump beam and pump-induced changes on the probe beam. Since the experiment measures the heterodyne beat signal of the probe and the reference, and terms that result in changes on the pump beam can be ignored. In addition, probe-induced changes on the probe beam are typically very small, since the probe beam power is usually at least 6 dB less than the pump power. Thus, probe-induced changes on the probe beam terms will also

be ignored. We will consider only the terms that include pump-induced changes on the probe beam, when the pump and the probe have parallel polarizations, which is the case in our experiments. The resulting change in probe intensity can be written as a sum of two terms [31, 37]:

$$\Delta I_{pr} = b(\gamma_{||} + \beta_{||}) \tag{4.5}$$

$$\gamma_{||}(\tau) = \int dtdt' |E_1(t-\tau)|^2 h_{xxxx}(t-t')|E_1(t)|^2$$

$$\beta_{||}(\tau) = \int dtdt' E_1^*(t-\tau)E_1(t)h_{xxxx}(t-t')E_1^*(t')E_1(t'-\tau)$$

where the field delayed by τ is the probe, and other other one is the pump. The term $\gamma_{||}(\tau)$ is a material response convolved with a second order correlation function (optical intensity), so it is the material response to the pump field, exactly what we are trying to measure. The term $\beta_{||}(\tau)$ constitutes a coherent coupling between the pump and the probe beams at zero time delay. It is evident from $\beta_{||}(\tau)$ expression that $\beta_{||} = 0$ when there is no overlap between the pump and the probe beams. Upon further examining Equation 4.5, it is evident that at zero time delay between the pump and the probe, $\beta_{||}(\tau = 0) = \gamma_{||}(\tau = 0)$, which means that at zero time delay, half of the measured HPP response is due to the actual material response, and another half is due to the coherent artifact. Therefore, all the data must be normalized to account for this.

4.2 Experimental Setup

The schematic of the experimental setup of the heterodyne pump-probe experiment used to measure TiO_2 devices is shown in Figure 4-2. The optical beam starts with Spectra Physics optical parametric oscillator (OPO) OPAL pumped by titanium-sapphire MaiTai laser. The resulting beam is a 80 MHZ train of optical pulses, centered at 1550 nm, with pulse duration of $\sim 180fs$. The beam passes through a half-waveplate and a polarizing beam splitter cube (PBS_1 in Figure 4-2), which separates the probe beam and the future pump/reference beam. HWP-PBS combination allows to tune the power in both beams. The probe path passes through an AOM, and is upshifted by Ω_1=36.7MHz. The beam then goes through another HWP (which allows to tune the power in the probe beam incident on the sample independently from the pump/reference beam powers), and is recombined with the pump using a 50/50 beam splitter cube. The pump beam, after passing through PBS_1, goes through another HWP/PBS combination, which separates it into the pump and the reference beams. The pump is reflected off PBS_2 as shown in Figure 4-2, passes through a mechanical chopper (Ω_c=1.3kHz), a variable time delay stage, another HWP, which allows to tune the pump power incident on the sample independently, and is combined with the probe beam in a 50/50 beam splitter. Combined pump and probe beams pass through PBS_3 in order to ensure they have the same exact polarization state, followed by a combination of QWP and HWP for polarization tuning, and are coupled into TiO_2 waveguide using a free space objective. An identical free space objective couples the light out of the waveguide into the 50/50 fiber splitter, which combines the pump-probe beam with the reference beam. The reference beam, after being separated from the pump at PBS2, passes through another AOM, which upshifts the beam by Ω_2=35MHz, followed by a variable time-delay stage which allows to match the reference and the probe path signals, in order to overlap the two

on the fast photodetector. This beam then goes through a QWP/HWP combination, is coupled into an SMF28 optical fiber, and is combined with the pump and the probe beams using a 50/50 fiber power splitter/combiner. One output of this power splitter is used to monitor the optical power in either one of the beams, while the other end is directed into a fast photodetector. The probe and the reference beams beat at the photodetector with $\Omega_b = \Omega_1 - \Omega_2 = 1.7MHz$. A low pass RF filter follows the photodetector and cuts off all the RF frequencies above 1.9 MHz. The RF signal from the photodetector goes into the IC-R71A Ham radio, which can be set at either AM or FM mode depending on the measurement type. The demodulated signal from the Ham radio is directed into the lock-in amplifier, which locks onto the pump chopping frequency, and thus detects only pump-induced changes on the probe-reference beat signal. In order to couple the light into and out of the waveguide, two identical free space objectives were used (60X,NA=0.85). We note that prior to entering the TiO_2 waveguide, both the pump and the probe beams travel using free space optics, which adds negligible dispersion to the optical pulse. An acousto-optic modulator in the probe path does not add significant dispersion to the probe beam either. In order to get a proper beat signal at the photodetector, both the reference and the probe beams are length matched, and polarization matched. This is done by first varying the QWP/HWP combination in the pump-probe path in order to find the polarization state best supported by the device, and then varying the QWP/HWP combination in the reference path in order to match the polarization at the output of the TiO_2 waveguide. When polarization states of the probe and the reference beam are identical, the strength of the beat signal on the detector is maximum.

Since the Ham radio is used in order to demodulate the signal, it is necessary to properly calibrate the radio to make sure it operates in the linear regime. This is done using the

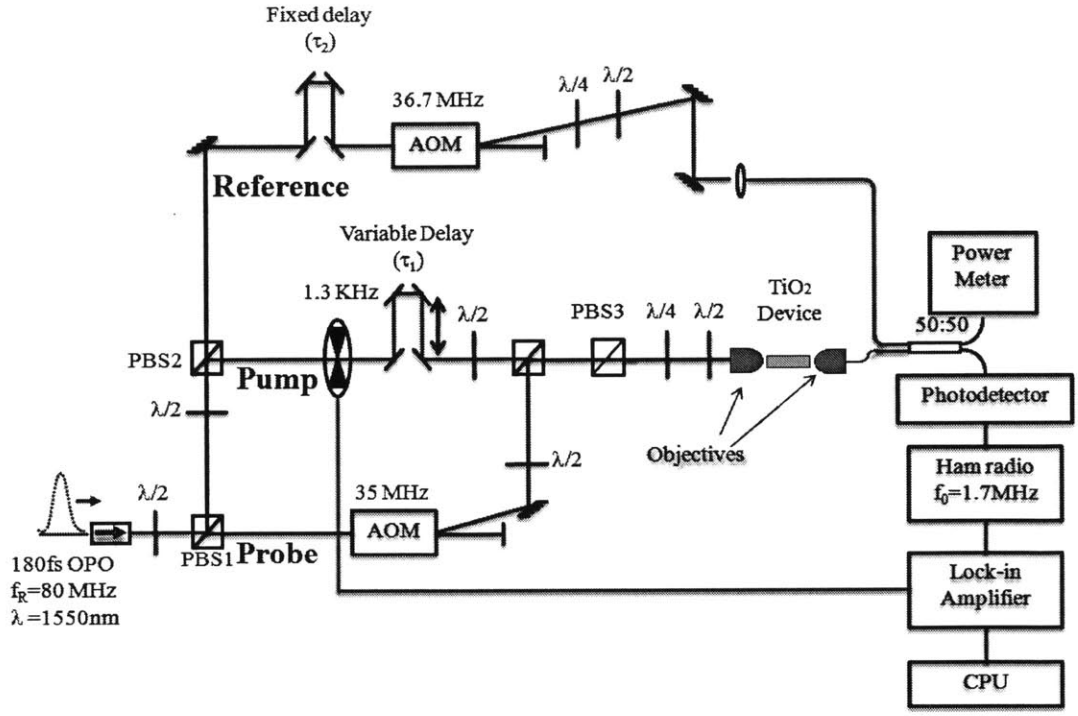

Figure 4-2: Heterodyne pump-probe setup.

following procedure: first, the level of the probe-reference beat signal is measured. Second, a separate RF signal of the same level as the probe-reference beat signal is created by a separate signal generator, and varying degrees of AM and FM modulation level are applied to this RF signal externally. The response of the radio in AM/FM regimes should scale linearly with linear change in AM/FM modulation depth on the signal. The level of the RF signal going into the radio is therefore attenuated until the response of the radio is linear for 100% AM and 300% FM modulation depths.

Separately, the radio is checked for any undesired AM/FM conversion. Both RF and AF gains on the radio are adjusted until a 100% AM modulated signal shows no component in FM demodulation, and a 100% FM modulatated signal shows no component in AM demodulation.

4.3 Characterizing coupling losses

The response of the waveguide to the excitation by an ultrafast pulse depends on the light intensity inside the waveguide. Our experimental setup lets us measure the light power prior to entering the input objective (by using a free space power meter), and after exiting the output objective (by using fiber-coupled power meter). Thus, the actual light power inside of the waveguide is not known, and needs to be determined by carefully analyzing the coupling losses. While it is most simple to assume that our input and output coupling losses are equal, careful previously demonstrated analysis has shown that the difference of such coupling losses may be as large as 4 dB [2, 38]. In addition, it was visually observed that our particular waveguides were not cleaved properly, and the input and output facet cleaves differed significantly when observed via microscope. Therefore, it is important to separate the input and the output coupling losses and determine them without the assumption that they are equal.

A schematic that visualizes coupling losses is shown in Figure 4-3. The optical beam enters the waveguide, with optical power right before the waveguide being P_{in}, in dBm. Optical power after exiting the waveguide is measured to be P_{out}, also in dBm. C_1 is the fractional input coupling loss, measured in dB, and C_2 is the fractional output coupling loss, measured in dBm. When the direction of light propagation is changed, C_2 becomes the input loss, and C_1 becomes the output loss, but they retain the same fractional value. With no nonlinearities present, the losses can be described according to Equation 4.6, where α is a linear loss in dB/cm, and L is the device length in cm. The sum of coupling losses can then be determined by measuring the input and output power in the linear regime, according the Equation 4.7. In order to calculate coupling losses individually, another, different equation, relating C_1 and C_2 is necessary.

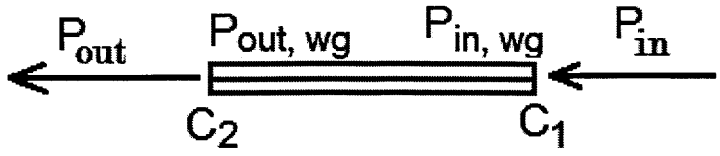

Figure 4-3: Schematic of coupling losses in and out of the waveguide.

$$P_{out} = P_{in} - C_1 - C_2 - \alpha L \tag{4.6}$$

$$C_1 + C_2 = P_{in} - P_{out} - \alpha L \tag{4.7}$$

In a similar work performed on the silicon nanowaveguides by A. R. Motamedi [38], the coupling losses have been separated using two photon absorption nonlinearity. The power transmitted through any particular waveguide would decrease and deviate from the linear response on a log-log scale as the input power is increased to the point where two photon absorption effects become significant. The level of this two-photon absorption depends on the optical power inside of the waveguide. The experiment is performed in two directions, with light propagating through the waveguide right-to-left, and left-to-right, and the two-photon-absorption-dependent loss is measured in each case. The difference between two power values for two measurement directions that exhibit the same two-photon absorption corresponds to the difference in the input and output coupling losses.

TiO_2 waveguides used in this experiment do not support two photon absorption at 1550 nm, and thus it can not be used to separate coupling losses. The only other way to measure such coupling losses is to use some other type of nonlinearity, that is dependent on the light intensity inside of the waveguide. In this work, we will use pump-induced phase

modulation of the probe beam as such nonlinearity. In fact, the main normalized heterodyne pump-probe response curve from PM measurement is exactly the data that will be used to characterize coupling losses. Figure 4-4 (a) shows PM heterodyne pump-probe traces for the light propagation from left to right, for various input power levels. The maximum peak in each curve corresponds to point where the probe and the pump pulses have maximum time-overlap. The peak value on each curve corresponds to the maximum phase modulation induced by a certain light intensity inside of the waveguide. The PM heterodyne pump-probe experiment was subsequently repeated with light propagating right-to-left through the same waveguide. The results are shown in Figure 4-4 (b). Figures 4-4 (a) and (b) show the same experiment, with exactly the same input pump power, performed in two different directions. It is evident from the two plots that, for the same input pump power, the maximum phase modulation on the probe signal is lower for right-to-left light propagation experiment. This can be explained with the difference in coupling losses - for the right-to-left direction, the input coupling loss is greater than the input coupling loss for the left-to-right light propagation. Thus, the difference between coupling coefficients C_1 and C_2 can be extracted from Figures 4-4 (a) and (b). We note that careful optical alignment is performed in those experiments to ensure that the same amount of light enters the input objective in either light propagation direction, and that the amount coupled in is maximized.

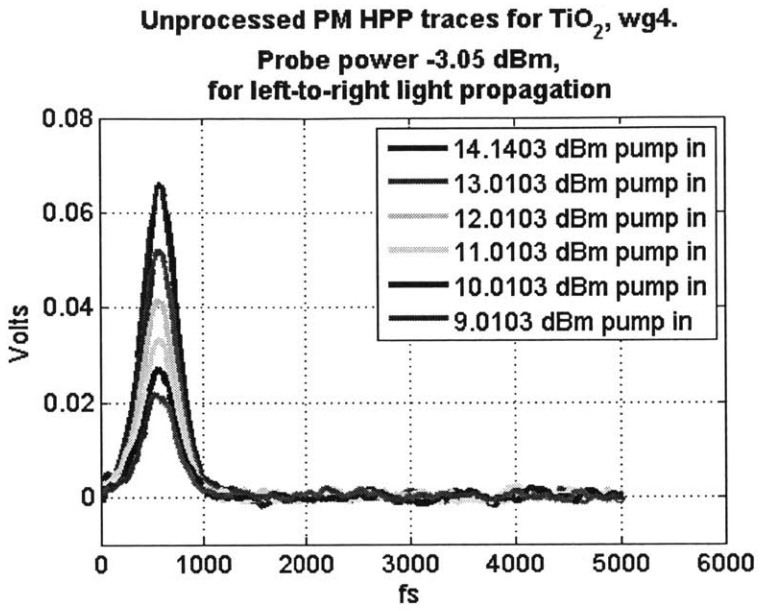

(a) HPP PM measurement traces, unprocessed, for for left-to-right light propagation.

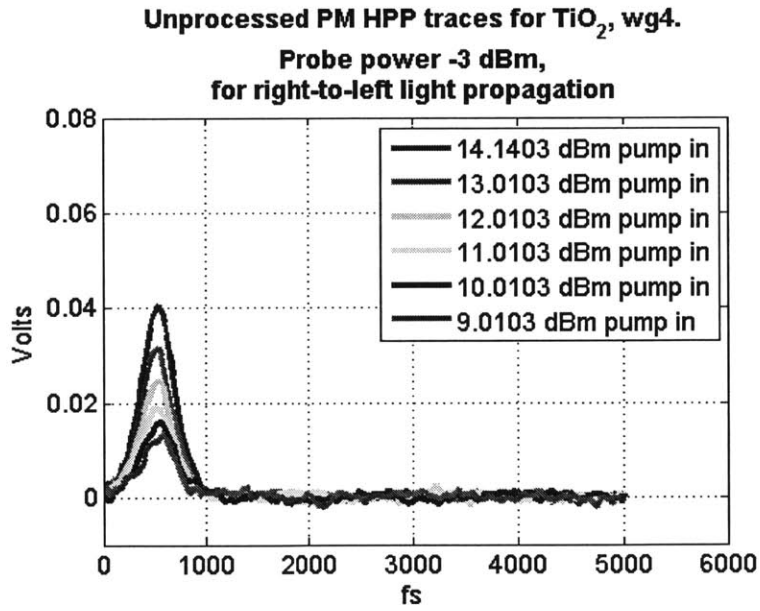

(b)HPP PM measurement traces, unprocessed, for right-to-left light propagation.

Figure 4-4: Heterodyne pump-probe PM measurement traces, unprocessed, for for left-to-right (top) and right-to-left (bottom) light propagation direction.

In order to extract the difference between the coupling coefficients from the phase modulation heterodyne pump-probe measurements, we first plot the maxima of the HPP response versus input pump power (the peak of each plot in Figure 4-4 vs input pump power). This is shown in Figure 4-5 (a). This maximum HPP response (maximum phase modulation) is proportional to the change in optical phase. This change in optical phase is shown in Figure 4-5 (b), with the detailed calculations of the phase from maximum HPP phase modulation response curves explained in Section 4.4. Next, the procedure is to find the points on the left-to-right curve of Figure 4-5 that have exactly the same phase modulation as the points on the right-to-left curve. In order to do that, both curves are extrapolated to have more data points, and Matlab algorithm is used to find the desired points, which are shown in Figure 4-6 with large black crosses. At such points, the change in optical phase is the same for both light propagation directions; therefore, optical intensity inside of the waveguide must also be the same for both directions of propagation. Since the points of equal optical phase change corresponding to two light propagation directions clearly correspond to different input optical power, the difference between this input optical power for two propagation directions must come from the difference in coupling losses.

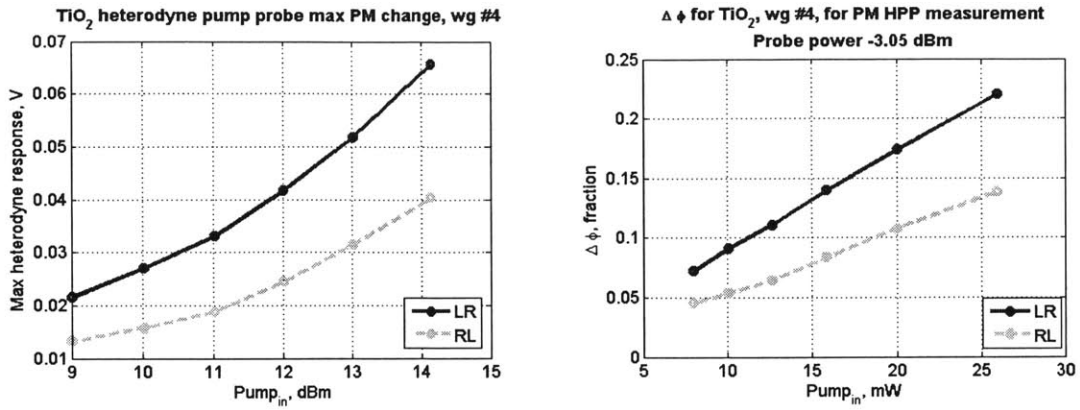

(a) (b)

Figure 4-5: (a) Maximum response of the heterodyne pump-probe PM measurement for left-to-right (LR) and right-to-left (RL) light propagation directions. (b) Maximum probe phase change due to pump-induced index change, for left-to-right (LR), and right-to-left (RL) light propagation directions.

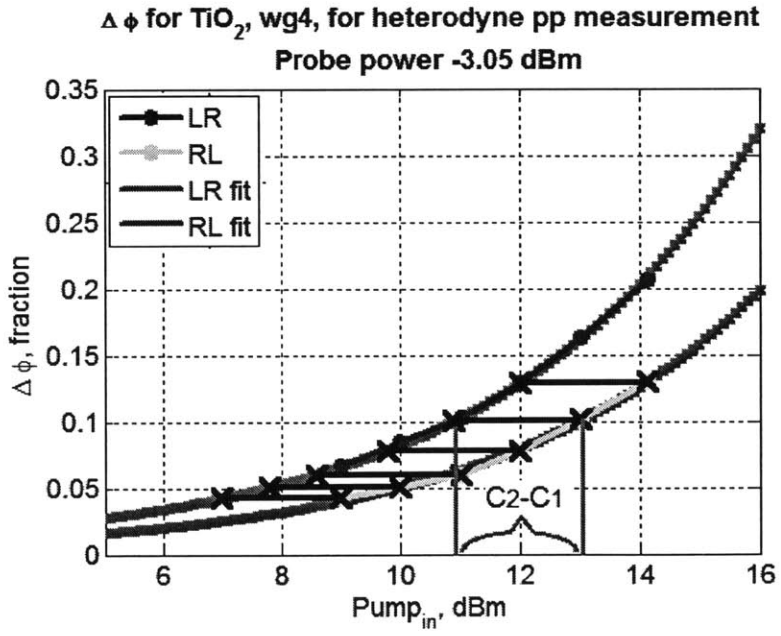

Figure 4-6: Determining $C_2 - C_1$ from maximum phase change on HPP response curved for two directions of light propagation. Black crosses / lines show points of equal phase change in both directions of light propagation.

Final sum and difference of coupling losses versus input pump power are shown in Figure 4-7. From this data, average coupling losses are calculated to be $C_1 = 10.93dB$, $C_2 = 13.12dB$.

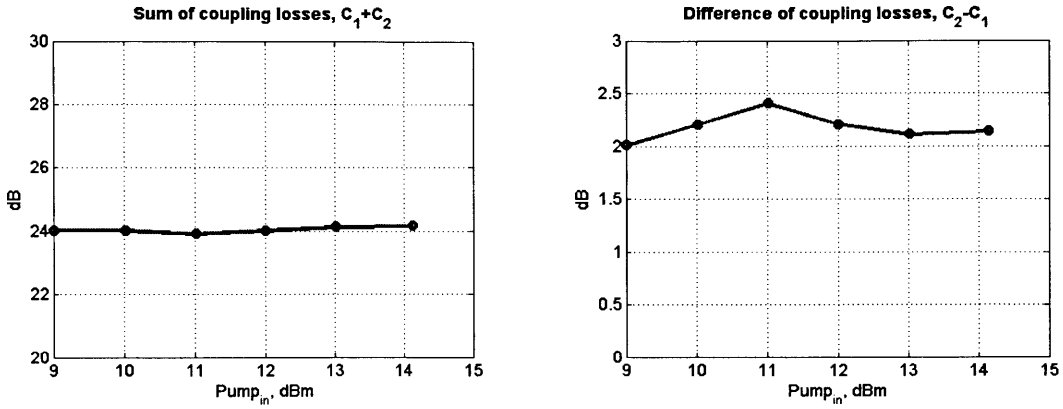

(a) (b)

Figure 4-7: (a) Sum of coupling losses for TiO_2 waveguide 4. (b) Difference of coupling losses for TiO_2 waveguide 4.

4.4 Phase Modulation (PM) measurement

Pump-induced changes in optical phase of the probe beam can be extracted from the phase modulation heterodyne pump-probe experiments. Such measured phase changes could then be related to the nonlinear Kerr coefficient. In order to extract the phase changes and the nonlinear parameters, heterodyne pump-probe data must be properly normalized, and the results should be carefully examined. We note here that the analysis is somewhat more simple if the waveguides under study exhibit negligible dispersion. For the waveguides studied in this thesis, the dispersion at 1550 nm is -2200ps/nm km), which should be included in the interpretation of the results.

4.4.1 PM normalization

Figure 4-2 shows the schematic of the heterodyne pump-probe experiment. In phase modulation experiment, the HAM radio is set to FM mode, such that it extracts the frequency modulation of the probe signal induced by the pump signal. The lock-in amplifier integrates the signal over time, and provides background-free measurement by using the pump chopping frequency as a reference signal. Time-integration converts frequency modulation into phase modulation, which is used to obtain the nonlinear refractive index. The units of the unprocessed data coming out of the lock-in amplifier are mV. In order to convert mV to fractional change in optical phase, a careful calibration of the setup is performed to determine the phase modulation reference signal. For angular modulation, the modulation index is defined according to Equation 4.8, where Δf_p is the maximum frequency deviation, f_m is the frequency of the modulating signal, and $\Delta\phi_p$ is phase change in radians. In order to obtain one radian, the Δf_p must be equal to f_m. In heterodyne pump probe experiments, the modulating frequency is the frequency that the pump is being chopped at, in our case, 1.3kHz. Thus, for 1 radian of phase change, 1.3kHz of maximum frequency deviation must be applied to the signal.

$$m_{FM} = \frac{\Delta f_p}{f_m} = \Delta\phi_p \tag{4.8}$$

This calibration is done according to the following procedure:

1. The pump beam is blocked

2. The AOM that frequency-shifts the probe beam is driven by an RF source with $\Omega = 36.7MHz$, as for the normal experiment, however, the 36.7 MHz carrier going into the AOM is also modulated by the square wave at a frequency of f_m=1.3kHz,

which coincides with the pump chopping frequency; and Δf_p, the maximum shift of Ω, is set to 1.3kHz, in order to provide 100% FM signal, or 1 radian of maximum phase modulation. This provides 100% phase modulation (or a maximum phase change of 1 radian) of the optical signal.

3. This 100% FM modulated probe signal beats with the reference signal. The beat signal is directed into a fast detector, which directs the RF beat signal (at 1.7MHz) into the HAM radio, set for FM demodulation mode, with a carrier frequency set to 1.7MHz.

4. The output of the radio is directed into the lock-in amplifier, which takes the 1.3kHz modulating frequency as a reference.

5. The resulting R value from the lock-in amplifier is used as a 100% PM (1 radian) reference value.

Figure 4-8 shows the 100% FM modulated beat note of the probe and the reference, as a result of this normalization. The signal was measured at the fast detector collecting probe/reference beat note. In this Figure, the central beat peak is at 1.7MHz, and the side bands are separated from each other by 1.3kHz, which is the modulating frequency, equal to the chopper frequency. The height difference of the adjacent peaks refelects the level of the FM modulation, and can be analytically calculated for any m_{FM} value [39]. Although an identical trace could be obtained through heterodyne pump-probe experiment with an appropriate amount of input pump power, we found that, with measured material nonlinearity values, the maximum pump power level available in the setup was not enough to exceed 0.3 radians of phase change, far from 1 radian obtained through this calibration. Since neither the reference nor the probe power levels change throughout the experiment,

this 100% probe phase modulation is independant of the input pump power, and is used to normalize all the PM heterodyne pump-probe traces. After normalization, the heterodyne response is the fractional pump-induced phase change($\Delta\phi$) on the probe. Figure 4-9 shows a heterodyne pump-probe trace, fully normalized, accounting for the coherent artifact described in Section 4.1.3, versus pump power in the waveguide.

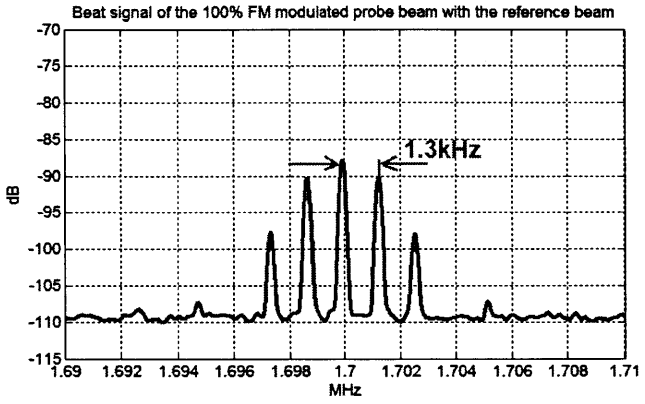

Figure 4-8: RF beat signal of 100% FM modulated probe beam and the reference beam, used for PM normalization.

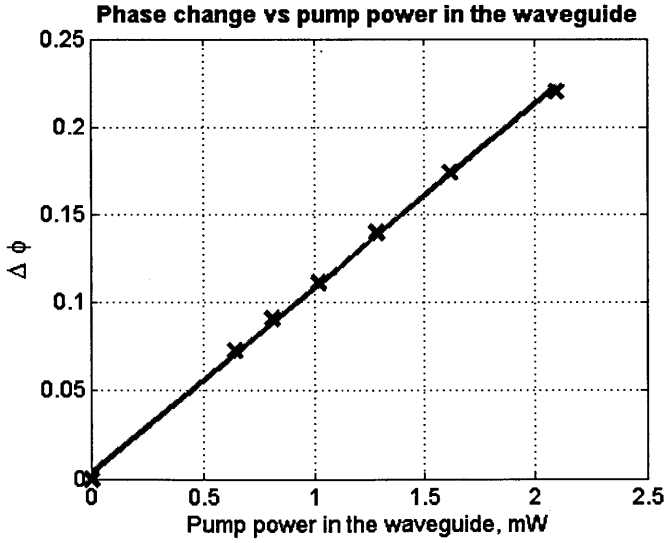

Figure 4-9: Normalized heterodyne pump-probe material response for PM measurement, versus pump power in the waveguide

4.4.2 Calculating nonlinear index of refraction from $\Delta\phi$.

The heterodyne pump-probe experiment measures changes in optical phase of the probe beam, induced by the pump beam. Equation 3.2 relates this change in optical phase to the nonlinear refractive index coefficient n_2, assuming no dispersion. Thus, n_2 can be written according to Equation 4.9, where λ_0 is the center wavelength of the laser in vacuum, I is the effective light intensity inside of the waveguide, $\Delta\phi$ is the peak phase change due to nonlinearity, and L_{eff} is the effective length of the interaction, which takes into account linear losses of the material. For negligible dispersion, the effective length is calculated according to Equation 4.10, where L is the physical length of the device, and α is the linear loss. For the TiO_2 devices measured in this thesis, $\alpha = 8dB/cm$, and L=9.2mm, which gives the effective length of 4.43mm.

$$n_2 = \Delta\phi \left(\frac{1}{I}\right) \frac{\lambda_0}{2\pi} \frac{1}{L_{eff}} \tag{4.9}$$

$$L_{eff} = \frac{1 - e^{-L\alpha}}{\alpha} \tag{4.10}$$

The effective intensity of the optical beam is calculated by dividing the peak pulse power by the effective area. For $sech^2$ pulse shape, the peak power is calculated from the average power as follows: $P_{peak} = 0.88\frac{P_{av}}{\tau_p R}$, where R is the repetition rate of the laser, and τ_p is the FWHM pulse width. Because the devices measured exhibit significant amount of normal dispersion, the pump and the probe pulses broaden inside of the waveguide. The effective pulse width, to be used in the calculations, can either be determined from the split-step analysis, or estimated from the heterodyne pump-probe plots. Figure 4-4 shows unnormalized HPP traces, where each trace can be describes as a convolution

of the intensity autocorrelation with the material response (as described by $\alpha_{||}$ term in Equation 4.5). Assuming instantaneous material response, the heterodyne pump-probe traces can be thought of as scaled versions of the intensity autocorrelation. We estimate the FWHM nonlinear effective duration of the pulse from the intensity autocorrelations to be $\sim 260fs$ on average. In comparison, optical pulses at the input of the waveguide have a FWHM duration of 180fs; therefore, the measured pulse duration of $260fs$ indicates the definite pulse spreading inside of the waveguide, which affects the nonlinear phase. In order to take into account for the dispersion in the waveguides, we therefore use the pulse duration of $260fs$ in order to calculate optical intensity, when using the Equation 4.9 to calculate nonlinear refractive index. The effective area of the optical mode for the nonlinear interaction is calculated according to the following formula [40]:

$$A_{eff} = \frac{Z_0^2}{n_{core}^2} \frac{\left| \int \int Re\left\{E(x,y) \times H^*(x,y)\right\} \cdot e_z dxdy \right|^2}{\int\int_{core} |E(x,y)|^4 dxdy} \tag{4.11}$$

This formula assumes that the nonlinearity is limited to, and is uniform over, the core of waveguide. In low-index-contrast devices, Equation 4.11 reduces to a more standard effective area definition [41].

For the TiO_2 devices measured in this work, A_{eff} was calculated to be 0.373 μm^2. We note that the pump-probe experiment measures the average change in optical phase, where the measured phase change is the result of the time-overlap integral of the pump and the probe, weighted by the peak phase change. Equation 4.9 assumes $\Delta\phi$ is the peak phase change, not the average phase change. Taking into the account the time-overlap integral of the sechant hyperbolic pulses weighted by the peak phase change, the measured phase change is about a factor of two less than the peak phase change. Figure 4-10 shows $\Delta\phi_{peak}$ versus optical intensity inside of the waveguide, where the intensity is in units of

$W/cm^2 \times 10^{10}$. The slope of this measured curve is the proportionality constant between $\Delta\phi$ and n_2: $\Delta\phi = slope \times n_2$. This slope, extracted from the linear fit in Figure 4-10, was used to calculate nonlinear refractive index n_2, which is found to be $1.03 \times 10^{-15} cm^2/W$.

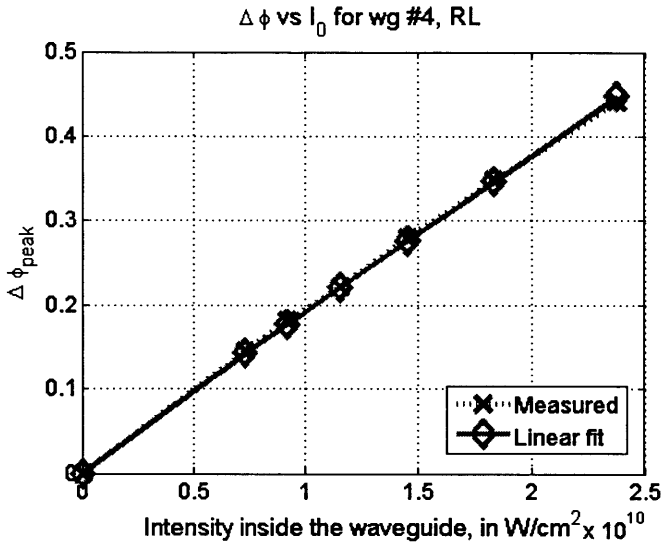

Figure 4-10: Measured nonlinear peak phase change versus peak optical intensity inside of the waveguide

In our calculations, we assumed that Equation 4.9 could be used for calculating optical Kerr coefficient in waveguides with significant amount of dispersion, provided that the pulse duration used for calculations is the dispersion-broadened value. In order to verify that such calculations are correct, we run the split-step simulation code [34] (see code attached in Appendix), that takes into account both nonlinearity and dispersion. The split-step code starts with a pulse width of τ_p=180fs, and the average input pump pulse energy equal to 26.2pJ (corresponding to the actual input power in the waveguide). The code then step-by-step propagates the pulse through the duration of the waveguide, adding the nonlinearity in the time domain and the dispersion in the frequency domain. With $n_2 = 1.03 \times 10^{-15} cm^2/W$, we get the maximum peak nonlinear phase shift of 0.45 radians, which

agrees very well with the measured peak nonlinear phase change of $\Delta\phi = 0.441$ radians, as shown in Figure 4-10. Moreover, the pulse duration at the end of the effective length period of the waveguide (i.e. at 4.43 mm point) also agrees with the measured pulse duration. We therefore conclude that according to our heterodyne pump probe measurements, the optical Kerr coefficient of anatase is measured to be $1.03 \times 10^{-15} cm^2/W$.

4.5 Amplitude modulation (AM) measurement

Heterodyne pump-probe AM measurements detect changes in the probe signal amplitude that are due to the pump-induced nonlinear absorption. Multi-photon absorption is a nonlinear process, which depends on the input signal power. Usually, if the material energy gap supports two-photon absorption, a heterodyne pump probe experiment allows to determine the TPA coefficient, along with TPA-induced free-carrier absorption (FCA). We note that TiO_2 devices studied in this thesis do not support two-photon absorption at 1550nm, and thus, no AM signal was detected at the output of the waveguide. To confirm this, we present a brief analysis along with one trace showing no AM signal for the highest input pump power supported by the setup.

4.5.1 AM normalization

AM measurements in heterodyne pump-probe experiments need to be normalized to the AM reference level. The degree of modulation m, for an AM signal, is defined according to Equation 4.12 below, where E_{max} is the maximum signal amplitude, and E_{min} is the minimum signal amplitude. With 100% AM modulation, m=1, and the signal goes completely on and off at the modulating frequency. The reference level is obtained by blocking the pump, and chopping the probe beam instead at the pump chopping frequency (1.3kHz in

our experiment). The chopper, with 50% duty cycle, creates 100% AM modulation at the chopping frequency. The response of the HAM radio in the AM regime to the beat signal of the reference beam and the chopped probe beam is fed into the lock-in amplifier, which uses the chopping frequency as a reference signal. The value from the lock-in amplifier is used as a reference level for the AM measurement. Figure 4-11 shows the RF beat signal for the probe and the reference with 100% AM modulation used to determine the reference level. For AM modulation, the sidebands are separated from each other by the modulating frequency, which is evident in Figure 4-11, where the sidebands are separated from the carrier of 1.7MHz by f_m=1.3kHz. In addition, for 100% AM modulation, the sidebands closest to the carrier (at $f_c \pm f_m$) are 6dB lower than the carrier level, which is well indicated in Figure 4-11.

$$m_{AM} = \frac{E_{max} - E_{min}}{E_{max} + E_{min}} \tag{4.12}$$

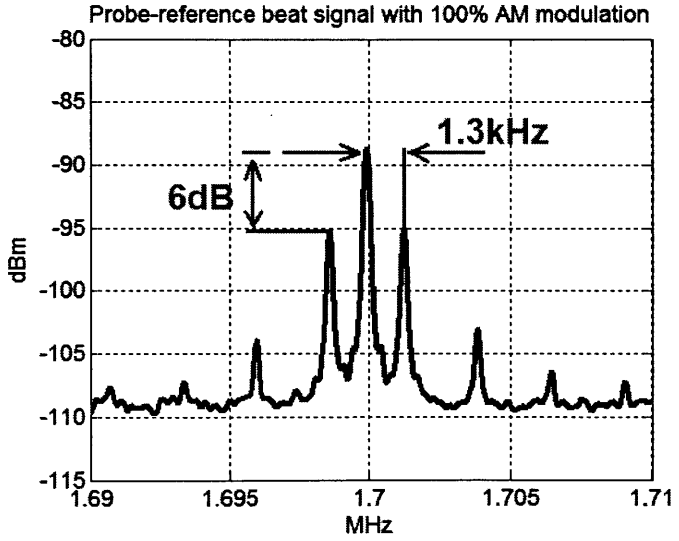

Figure 4-11: Probe-reference beat signal at 100% AM modulation, used to determine AM reference level.

4.5.2 Nonlinear absorption

Since the devices used in this work do not support two-photon absorption, no distinguishable AM trace was detected. An example of the measured heterodyne pump-probe trace in AM regime for TiO_2 waveguides, equivalent to Figure 4-4 of the FM regime, is shown in Figure 4-12 (a). As a comparison, an AM HPP measurement on silicon nanowaveguides, which do exhibit TPA at 1550nm, is shown in Figure 4-12 (b) [2, 38]. In this Figure, it is evident that the magnitude of the AM response is proportional to the input pump power. The greater the input pump power, the greater the TPA-induced loss, visible as a signal drop at zero time-delay. In fact, the AM response from this Figure consists of two components - the instantaneous response, proportional to TPA coefficient, and the slow response, proportional to the free carrier absorption (FCA). The depth of this signal at zero time delay can be used to extract TPA coefficient β, and the slow time response can be related to the FCA effective cross-section, as shown in [2].

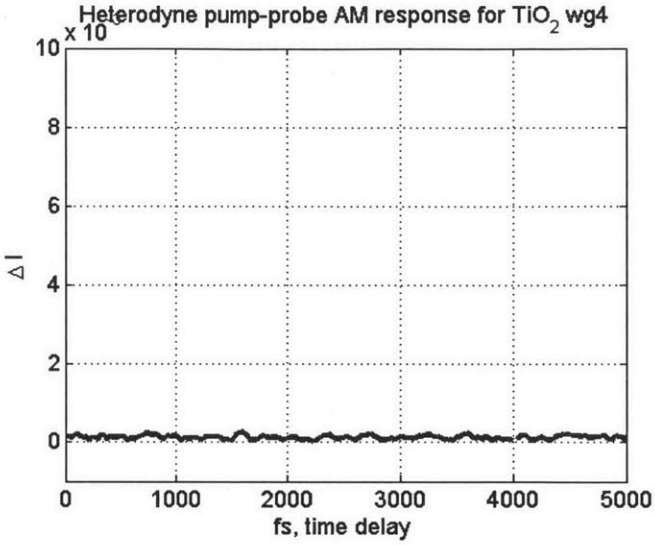

(a)

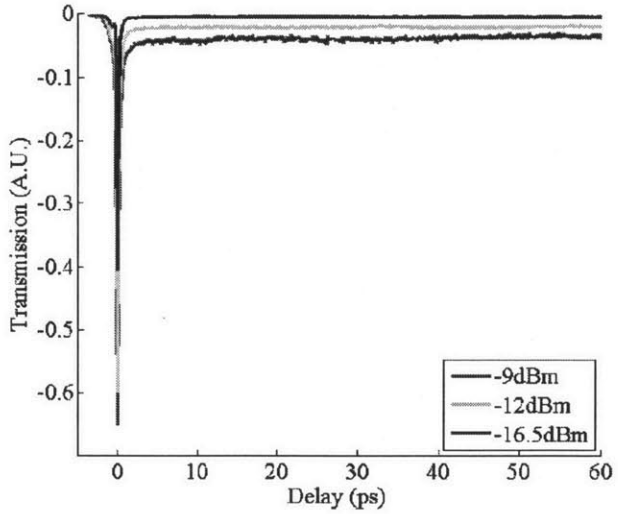

(b)

Figure 4-12: (a) AM response of the TiO_2 waveguide 4, shows no signal - no nonlinear absorption. (b) AM response of a silicon nanowaveguide, courtesy of A. Motamedi [2], shows a strong AM response due to a large TPA coefficient.

Chapter 5

Conclusion

For this thesis we have measured the optical Kerr nonlinearity of anatase titanium dioxide waveguides. We have used both the self-phase modulation method and heterodyne pump-probe methods to determine this nonlinearity. The SPM method resulted in $n_2 = 1.82 \times 10^{-15} cm^2/W$, while heterodyne pump-probe method resulted in $n_2 = 1.03 \times 10^{-15} cm^2/W$, which is a factor of 1.767 smaller than the SPM-measured value. Since the same waveguide was measured in two experiments, the values should not differ by such a large factor. In order to double-check the values measured, the identical split-step code was used in order to calculate the nonlinear phase shift for both experiments. The input pulse energy that was used in SPM experiment was used with SPM-measured n_2 value, and separately the input pulse energy that was used in HPP experiment was used with HPP-measured n_2 value. We found that in each case the split step code confirmed the maximum phase change directly measured by the experiment, which proves that each experiment is self-consistent. Table 5 summarizes the results of the experiments and the split-step code analysis.

Further studies are necessary to determine whether the optical Kerr coefficient of anatase TiO_2 is closer to $1.82 \times 10^{-15} cm^2/W$, or to $n_2 = 1.03 \times 10^{-15} cm^2/W$. If the true value for

	Input pulse energy	**Input intensity**	$\mathbf{n_2}$	**Measured** $\Delta\phi_{\mathbf{peak}}$	**Calculated** $\Delta\phi_{\mathbf{peak}}$
	pJ	W/m^2	cm^2/W	radians	radians
HPP	26.2	0.245×10^{15}	1.03×10^{-15}	0.44	0.451
SPM	229	3.0×10^{15}	1.82×10^{-15}	1.5π	1.5π

Table 5.1: Final results from both heterodyne pump-probe(HPP) and spectral broadening/self-phase modulation (SPM) experiments.

anatase TiO_2 n_2 is closer to the SPM-measured value, this makes the material comparable to silicon nitride, and the nonlinearity is indeed an order of magnitude higher than that of silica glass. On the other hand, if the true n_2 value is closer to that measured by heterodyne pump-probe experiment, this may make the anatase TiO_2 slightly less attractive. Future experiments are planned to resolve this difference.

Bibliography

[1] C. C. Evans, J. D. B. Bradley, J. Choy, O. Reshef, P. B. Deotare, M. Loncar, and E. Mazur, "Submicrometer-width TiO_2 waveguides," *Proc. CLEO: Science and Innovations*, (San Jose, CA), May 2012.

[2] A. R. Motamedi, A. H. Nejadmalayeri, A. Khilo, F. X. Kartner, and E. P. Ippen, "Ultrafast nonlinear optical studies of silicon nanowaveguides," *Optics Express* **20**(4), pp. 4085–4101, 2012.

[3] M. Dahlem, *Studies of advanced integrated nano-photonic devices in silicon.* PhD thesis, Massachusetts Institute of Technology, 2011.

[4] M. Salib and et al, "Silicon photonics," *Intel Technology Journal* , pp. 1–20, May 2004.

[5] W. Green, S. Assefa, A. Rylyakov, C. Schow, F. Horst, and Y. Vlasov, "CMOS integrated silicon nanophotonics: Enabling technology for exascale computational systems," *Invited talk at the SEMICON Conference*, (Tokyo, Japan), December 2010.

[6] Y. A. Vlasov, "Silicon CMOS-integrated nano-photonics for computer and data communications beyond 100G," *IEEE Communications Magazine* , pp. 567–572, February 2012.

[7] A. Khilo and et al, "Photonic ADC: Overcoming the bottleneck of electronic jitter," *Optics Express* **20**(4), pp. 4454–4469, 2012.

[8] Q. Lin, J. Zhang, G. Piredda, R. W. Boyd, P. M. Fauchet, and G. P. Agrawal, "Dispersion of silicon nonlinearities in the near infrared region," *Applied Physics Letters* **91**(021111), 2007.

[9] Q. Lin, O. J. Painter, and G. P. Agrawal, "Nonlinear optical phenomena in silicon waveguides: Modeling and applications," *Optics Express* **15**(25), pp. 16604–16644, 2007.

[10] O. Carp, C. L. Huisman, and A. Reller, "Photoinduced reactivity of titanium dioxide," *Progress in Solid State Chemistry* **32**, pp. 33–177, 2004.

[11] S. J. Wang, W. T. Chang, J. Y. Ciou, M. K. Wei, and M. S. Wong, "Preparation of TiO_2 thin films by laser ablation for photocatalytic applications," *Journal of Vacuum Science and Technology A* **26**(4), pp. 898–902, 2008.

[12] A. Fujishima, T. N. Rao, and D. A. Tryk, "Titanium dioxide photocatalysis," *Journal of Photochemistry and Photobiology C* 1(21), pp. 898–902, 2000.

[13] A. Fujishima and X. Zhang, "Titanium dioxide photocatalysis: present situation and future approaches," *Comptes Rendus Chimie* **9**(5-6), pp. 750–760, 2006.

[14] J. N. Clifford, E. Martinez-Ferrero, and E. Palomares, "Dye mediated charge recombination dynamics in nanocrystalline TiO_2 dye sensitized solar cells," *Journal of Materials Chemistry* **22**(12), pp. 415–422, 2012.

[15] I. Haeldermans, K. Vandewal, W. D. Oosterbaan, A. Gadisa, J. D'Haen, M. V. Bael, J. V. Manca, and J. Mullens, "Ground-state charge-transfer complex forma-

tion in hybrid poly(3-hexyl thiophene):titanium dioxide solar cells," *Applied Physics Letters* **93**(223302), 2008.

[16] H. A. Maclead, *Thin-film optical filters*, CRC Press, Boca Raton, Florida, 2010.

[17] J. D. B. Bradley, C. C. Evans, J. T. Choy, O. Reshef, P. B. Deotare, F. Parsy, K. C. Phillips, M. Loncar, and E. Mazur, "Submicrometer-wide amorphous and polycrystalline anatase TiO_2 waveguides for microphotonic devices," *Optics Express* , 2012. Submitted for publication.

[18] C. C. Evans, J. D. B. Bradley, E. A. Marti-Panameno, and E. Mazur, "Mixed two- and three-photon absorption in bulk rutile TiO_2 around 800 nm," *Optics Express* **20**, pp. 3118–3128, 2012.

[19] H. Long, G. Yang, A. P. Chen, Y. H. Li, and P. X. Lu, "Femtosecond z-scan measurements of third-order optical nonlinearities in anatase TiO_2 thin films," *Optics Comminucations* **282**, pp. 1815–1818, 2009.

[20] H. Long, A. P. Chen, G. Yang, Y. H. Li, and P. X. Lu, "Third-order optical nonlinearities in anatase and rutile TiO_2 thin films," *Thin Solid Films* **517**, pp. 5601–5604, 2009.

[21] www.mazur.harvard.edu.

[22] T. Ohsaka, F. Izumi, and Y. Fukiki, "Raman spectra of anatase TiO_2," *Journal of Raman Spectroscopy* **7**, pp. 321–324, 1978.

[23] N. Daldosso, M. Melchiorri, F. Riboli, F. Sbrana, L. Pavesi, G. Pucker, C. Kompocholis, M. Crivellari, P. Bellutti, and A. Lui, "Fabrication and optical characterization of thin

two-dimensional Si_3N_4 waveguides," *Materials Science in Semiconductor Processing* **7**, pp. 453–458, 2004.

[24] D. Milam, "Review and assessment of measured values of the nonlinear refractive-index coefficient of fused silica," *Applied Optics* **37**(3), pp. 546–550, 1998.

[25] T. Kato, Y. Suetsugu, M. Takagi, E. Sasaoka, and M. Nishimuru, "Measurement of the nonlinear refractive index in optical fiber by the cross-phase-modulation method with depolarized pump light," *Optics Letters* **20**(9), pp. 988–990, 1995.

[26] M. Dinu, F. Quochi, and H. Garcia, "Third-order nonlinearities in silicon at telecom wavelengths," *Applied Physics Letters* **82**, p. 2954, 2003.

[27] A. D. Bristow, N. Rotenberg, and H. M. van Driel, "Two-photon absorption and Kerr coefficients of silicon for 850–2200nm," *Applied Physics Letters* **90**(19), p. 191104, 2007.

[28] H. K. Tsang and et al, "Optical dispersion, two-photon absorption and self-phase modulation in silicon waveguides at 1.5μm wavelength," *Applied Physics Letters* **80**, pp. 416–418, 2002.

[29] R. Espinola, J. Dadap, R. Osgood, S. McNab, and Y. Vlasov, "C-band wavelength conversion in silicon photonic wire waveguides," *Optics Express* **13**(11), pp. 4341–4349, 2005.

[30] K. Ikeda, R. E. Saperstein, N. Alic, and Y. Fainman, "Thermal and Kerr nonlinear properties of plasma-deposited silicon nitride/ silicon dioxide waveguides," *Optics Express* **16**(17), pp. 12987–12994, 2008.

[31] E. P. Ippen and C. V. Shank, "Techniques for measurement," *Ultrashort Light Pulses, Picosecond Techniques and Applications*, (New York:Springer), 1977.

[32] L. L. Hall, *Femtosecond Nonlinearites in InGaAsP Diaode Lasers.* PhD thesis, Massachusetts Institute of Technology, 1993.

[33] J. T. Gopinath, *Studies of Third-Order Nonlinearities in Materials and Devices for Ultrafast Lasers.* PhD thesis, Massachusetts Institute of Technology, 2005.

[34] A. M. Weiner, *Ultrafast Optics*, John Wiley and Sons, Hoboken, NJ, 2009.

[35] K. L. Hall, G. Lenz, E. P. Ippen, and G. Raybon, "Heterodyne pump-probe technique for time domain studies of optical nonlinearities in waveguides," *Optics Letters* **17**, pp. 874–876, 1992.

[36] K. L. Hall, G. Lenz, A. M. Darwish, and E. P. Ippen, "Subpicosecond gain and index nonlinearities in InGaAs diode lasers," *Optical Communications* **111**, pp. 589–612, 1994.

[37] Z. Vardeny and J. Tauc, "Picosecond coherence coupling in the pump and probe technique," *Optics Communications* **139**(6), pp. 396–400, 1981.

[38] A. R. Motamedi, *Ultrafast Nonlinear Optical Properties of Passive and Active Semiconductor Devices.* PhD thesis, Massachusetts Institute of Technology, 2011.

[39] Hewlett-Packard, "Amplitude and frequency modulation," *Test and Measurement, Application Note* **150-1**, 1989.

[40] C. Koos, L. Jacome, C. Poulton, J. Leuthold, and W. Freude, "Nonlinear silicon-on-insulator waveguides for all-optical signal processing," *Optics Express* **15**(10), pp. 5976–5990, 2007.

[41] G. P. Agrawal, *Nonlinear Fiber Optics*, Academic Press, Burlington, Massachusetts, 2007.

Appendix A

Split-step MATLAB code

```
%% Split step code
%
%This is a split step code used to calculate the effects of SPM and
%dispersion on the waveguides. Effective area of the waveguides is
%calculated separately. The code takes the following variables as the
%input:
%
%Pulse width
%Pulse shape
%Pulse intensity
%Waveguide length
%Waveguide linear loss
%Dispersion
%Kerr nonlinearity
%Wavelength
%
%The code produces time and frequency spectra, and calculates the nonlinear
%phase shift.
%
%
%Written by Katia Shtyrkova
%
%03/23/2011
%
%Changed on 01/22/2013
%Changed on 01/26/2013
%
% !!!!!!!!!!!!!!!!!! SWITCH PULSE SHAPE - Gaus or Sech  !!!!!!!!!!!!
```

```
%Change input intensity - from SPM to HPP experiments
%Change dispersion D depending on the wavelength
%Change wavelength

%% Initialize, FFT keeping track of everything
clear all
close all
clc

%
%create time vector

N=2056; %number of samples in time domain
time_span=6000;  %fs
delta_t=(time_span/N) % fs, step in time domain

b2=((time_span-delta_t)/2);
t_vec= (-b2:delta_t:b2).*10^(-15);

t_p=180; %pulse width in fs
t_p=t_p*10^(-15);

%create frequency vector
w_span=2*pi.*(1/(delta_t.*10^(-15)));  %fs
delta_w=w_span/N; % fs, step in time domain

w_b2=((w_span-delta_w)/2);
freq_vec= -w_b2:delta_w:w_b2;


%%%%%%%%%% CHANGE I HERE %%%%%%%%%%%%%%%%%%%%%%
% I_meas=4.244.*1e15; %W/m^2 %Max intensity for spectral broadening experiment
% I_meas=3.105.*1e15; %W/m^2 %Max intensity for SPM that gave good fits
% I_meas=5.14.*1e13;    %W/m^2, maximum pump power that ends up in the waveguide
I_meas= 0.245.*1e15; %HPP experiment

a0=sqrt(I_meas);
%% Choose pulse shape!
% pulse_shape='Gaussian'
pulse_shape='Sech';

switch pulse_shape
    case 'Gaussian'
        %parameter that defines Gaussian pulse
        tau_p=0.8496.*t_p;
        a=a0.*exp(-(t_vec.^2)./(tau_p.^2));
    case 'Sech'
        %parameter that defines the width of the sech pulse
```

```
        tau_p=t_p./1.763;
        %Original input pulse (field)
        a=a0*sech(t_vec./tau_p);
end
%% Set up fields

%%%%%%%%%%%%%%%%%% CHANGE LAMBDA HERE %%%%%%%%%%%%%%%
  lambda=1550; %wavelength in nm, for HPP
%   lambda=1565;  %wavelength for SPM, nm
    omega_0=2*pi*(3*10^8)/(lambda*10^(-9)); % in Hz

    E=a.*exp(-1j.*omega_0.*t_vec);

    I=(abs(E)).^2;

    %Plot the original intensity
    figure

    plot(t_vec,I,'LineWidth',3);
       grid on
       hold on
    title('Original pulse');

%% Dispersion / SPM Parameters
L=9.2;      %mm   length of the device
c=3*10^8;   %m/s
alpha=8;    %linear loss, dB/cm

alpha_lin=(alpha./4.3429).*100; %linear loss, per m

%%%%%%%%%%%%%%%% CHANGE D HERE %%%%%%%%%%%%%%%%%%%%%%%
D=-2200;     %ps/nm km %This is technically for HPP experiment,
                                                  %i.e. for 1550nm
% D=-2265.4;      %ps/nm km %This is technically for SPM experiment,
                                                  %i.e. for 1565nm
% D=0;


beta2=(-D.*(lambda).^2. / (2.*pi.*c)) ;    %beta2* dimensions correction factor
                                               % ps^2/m
                                           % positive beta2 - normal GVD
L=L.*10^(-3);   %m
psi2=-L.*beta2.*10^(-24);     %s^2

% n_2=1.82.*1e-15; %cm^2/W n2 as measured in SPM experiment
n_2=1.031e-015; %cm^2/W - HPP final version

% n_2=0;
```

```
% lambda is defined previously in nm

gamma=(n_2.*2.*pi./lambda).*1e5;
%% Split step process
z_vec=linspace(0.1,6,100);

del_z=z_vec(2)-z_vec(1);  %mm

del_z=del_z.*10^(-3);  %m

freq_vec=fftshift(freq_vec);
a_orig=a;
a=fftshift(a);

A_w=fft(fftshift(a));   %pulse spectrum
A_w_orig=A_w;

n_steps=round(L./del_z)
    L_total=0;%initialize length variable
        %del_z is in m!!!!!!!!!!!
for ic=1:n_steps/2
    % Step 1. FFT the pulse
            %This is done prior to the loop
    % Step 2. Add dispersion in w domain
        A_w=A_w.*exp(-1j.*beta2.*(freq_vec.*10^(-12)).^2.*del_z./2);
             figure(1)
                cla
                    f_vec2=fftshift(freq_vec);
                    A_w_d2=fftshift(A_w);
                    A_w_orig2=fftshift(A_w_orig);
                    kk=800;
                plot(f_vec2(kk:end-kk),abs(A_w_orig2(kk:end-kk)),...
                                        'b','LineWidth',3);
                 hold on
                plot(f_vec2(kk:end-kk),abs(A_w_d2(kk:end-kk)),...
                                        'r','LineWidth',3);
                    grid on
                xlabel('frequency, Hz');
                title('Step 1. Add D, Spectrum ');
                legend('Original pulse','Disp + SPM');
    % Step 3. Fourier Transform back to time!!!!
        a=ifft(A_w,N);
        % account for linear loss!
        a=a.*(exp(-0.5.*alpha_lin.*del_z));
        a_max(ic)=max(abs(a));
    % Step 4. Add SPM.
        a=a.*exp(-1j.*gamma.*((abs(a)).^2)*(del_z));
        del_phi(:,ic)=gamma.*((abs(a)).^2)*(del_z);
```

```
                figure(3)
                    cla
                    plot(t_vec,abs(a_orig),'b','LineWidth',3);
                    hold on
                    plot(t_vec,(abs(a)),'g','LineWidth',3);
                    ylim([0 a0]);
                    grid on
                    xlabel('time, s');
                    title('Step 4. Pulse in time, add SPM');
    %Step 5. FFT the pusle from time to frequency
        A_w=fft(a, N);
   L_total=L_total+del_z;

end
%% Plotting Final Intensities

figure(5)
        plot(t_vec,(abs(a_orig)).^2,'b','LineWidth',3);
           hold on
        plot(t_vec,((abs(a)).^2),'g','LineWidth',3);

        grid on
        xlabel('time, s');
        legend('Original pulse','Dispersion-broadened pulse');
    title('Final pulse in time, Intensity');

figure(6)
                plot(f_vec2(kk:end-kk),(abs(A_w_orig2(kk:end-kk))).^2,...
                                                    'b','LineWidth',3);
                 hold on
                plot(f_vec2(kk:end-kk),(abs(A_w_d2(kk:end-kk))).^2,...
                                                    'r','LineWidth',3);
                    grid on
                xlabel('frequency, Hz');
%                 ylim([0 0.5.*1e19]);
                title('Final pulse, frequency spectrum');
                legend('Original pulse','Disp + SPM');


%% FWHM Calculations

I_orig=(abs(a_orig)).^2;
I_out=(abs(a)).^2;
%find maximum of the input intensity

I_orig_max = I_orig(I_orig==max(I_orig));
I_orig_max=I_orig_max(1);
```

```
I_orig_half_max = I_orig( (abs(I_orig-0.5.*max(I_orig))==...
                                    min(abs(I_orig-0.5.*max(I_orig)) ) ));
I_orig_half_max =I_orig_half_max (1);
ind_I_orig_FWHM = find(I_orig ==I_orig_half_max);

I_orig_FWHM=t_vec(ind_I_orig_FWHM(2))-t_vec(ind_I_orig_FWHM(1));


%find maximum of the output field
I_out_max = I_out(I_out==max(I_out));
I_out_max=I_out_max(1);

I_out_half_max = I_out( (abs(I_out-0.5.*max(I_out))==...
                                        min(abs(I_out-0.5.*max(I_out)) ) ));
I_out_half_max =I_out_half_max (1);
ind_I_out_FWHM = find(I_out == I_out_half_max);

I_out_FWHM=abs(t_vec(ind_I_out_FWHM(1))).*2;

t_fwhm_in=I_orig_FWHM.*1e15; %fs
t_fwhm_out=I_out_FWHM.*1e15; %fs

pulse_broadening_ratio = t_fwhm_out./t_fwhm_in

figure(7)
        plot(t_vec,(abs(a_orig)).^2,'b','LineWidth',3);
           hold on
        plot(t_vec,((abs(a)).^2),'g','LineWidth',3);
     plot(t_vec(ind_I_orig_FWHM(2)), I_orig_half_max,'rx','MarkerSize',15);
     plot(t_vec(ind_I_orig_FWHM(1)), I_orig_half_max,'rx','MarkerSize',15);
        grid on
        xlabel('time, s');
    plot(t_vec(ind_I_out_FWHM), I_out_half_max,'mx','MarkerSize',15);
    plot(abs(t_vec(ind_I_out_FWHM)),I_out_half_max,'mx','MarkerSize',15);
    legend('Original pulse','Broadened Pulse',...
                            'FWHM of the original','FWHM of the broadened');
    title('final intensity, testing');
%% Some further phase analysis

 del_phi_total=sum(del_phi(:,:),2);
 max_del_phi=max(del_phi_total)
 sprintf('max phase shift is %f radian',max_del_phi)

%% Possible phase analysis to pick a particular phase shift:
% del_phi_total=zeros(size(del_phi(:,1)));
% for ic=1:n_steps
%     if max(del_phi_total)<2*pi
%         clear del_phi_total
```

```
%          del_phi_total=sum(del_phi(:,[1:ic]),2);
%          max(del_phi_total)
%          ic
%      end
% end
%
```